2

Micro-mechanical Logic for Field Produceable Gate Arrays

by

Manu Prakash

B.Tech., Computer Science and Engineering (2002)
Indian Institute of Technology, Kanpur

Submitted to the Department of Media Arts and Sciences
in partial fulfillment of the requirements for the degree of

Master of Science

at the

MASSACHUSETTS INSTITUTE OF TECHNOLOGY

February 2005

Author .....
Department of Media Arts and Sciences
September 2004

Certified by .....
Neil Gershenfeld
Associate Professor of Media Arts and Sciences
Thesis Supervisor

Accepted by .....
Andrew Lippman
Chairman, Departmental Committee on Graduate Students

Micro-mechanical Logic for Field Produceable Gate Arrays

By
Manu Prakash

Submitted to Media Arts and Sciences department in partial fulfillment of the requirements for the degree of Master of Sciences at
Massachusetts Institute of Technology
February 2005

Thesis Committee

Neil Gershenfeld ----------
Associate Professor of Media Arts and Scineces
MIT Media Laboratory
Thesis Advisor

Scott Manalis ----------
Associate Professor of Media Arts and Sciences
and Biological Engineering
MIT Media Laboratory
Thesis Reader

Todd Thorsen ----------
Assistant Professor of Mechanical Engineering
MIT
Thesis Reader

Micro-mechanical Logic for Field Produceable Gate Arrays

by

Manu Prakash

Submitted to the Department of Media Arts and Sciences, School of Architecture and Planning
on September 2004, in partial fulfillment of the
requirements for the degree of
Master of Science

Abstract

A paradigm of micro-mechanical gates for field produceable logic is explored. A desktop manufacturing system is sought after which is capable of printing functional logic devices in the field. A logic scheme which induces non-linearities via geometrical properties is considered. Logic devices in two-phase air-water fluid-dynamic system at micron scales are constructed.

A systematic study of non-linearities and relevant force fields in fluid dynamics at low Reynolds Number is undertaken. Viscous forces dominate inertial forces at low Reynolds Number flows at low pressure. Thus devices based on non-linear inertial effects at high Reynolds numbers can not be scaled down to micron-sizes. Bubble microfluidic logic gates are invented to tackle the above problem, thus producing low Reynolds Number logic in newtonian fluids. Various devices including AND/OR gates, NOT gate, nonvolatile bistable memory, shift registers and ON/OFF flow valves, based on this new scheme of bubble bubble interaction in microfluidic devices to induce non-linearity, are designed and characterized. On-chip bubble generators and annihilators are used for encoding and destroying information in bubble logic devices. Applications of the above described logic devices as a flow control strategy for droplet based Lab-on-chip devices is explored.

A simple to construct in-situ pressure sensor based on the principle of compressibility of an air bubble in microfluidic devices is invented. A scheme of controlled bubble/droplet movement in shift registers via pulsating pressure fields for precise temporal control of start of microfluidic reactions is proposed. Excimer laser micromachining of boro-silicate glass is developed to direct write 3D microfluidic structures. Laser ablation process using a ArF based 193nm laser for machining is characterized using laser confocal microscopy techniques. Single bubble cavitation induced by laser pulses is developed as a process for writing micro-bubbles at precise locations in microfluidic channels.

Thesis Supervisor: Neil Gershenfeld
Title: Associate Professor of Media Arts and Sciences

Acknowledgments

First and foremost I acknowledge my advisor, Neil Gershenfeld for his generosity, constant and enthusiastic support, shear excitement and encouragement and sharing his values in life.

I would sincerely like to thank everybody in Physics and Media, Nanoscale sensing, Momachines and Quanta research groups. I would like to thank Matt Reynolds for telling me what being an engineer means, Saul Griffith for sharing his passion as an inventor, Dave Mosely and Brian Chow for teaching me how to play with chemicals, Vikrant Agnihotri for being on the crease with me at cricket games, Ken Brown for sharing time on the laser, Thomas Burg for answering thousands of questions I would bring to him, Raffi Krikorian for encouraging me at every step, Ben Recht for playing great music in the office, Rehmi post for making the life in the lab so much fun, Yael Maguire and Ben Vigoda for those exciting discussions, Everett for being such a nice dog in the office. Special thanks to Sun-Xu, Amy Sun, Ara Knaian and Jason Taylor.

Also a note of thanks for Susan Murphy-Bottari, Michael Houlihan and Sherry Lassiter. Without you guys, there is no PHM.

I would also like to thank my parents, family and friends for their love and support. Special thanks to Akshi Singh, for sharing her world with me and bringing a smile to mine.

This research was supported by NSF Center for Bits and Atoms(CBA) NSF CCR-0122419.

Contents

List of Figures

List of Tables

Chapter 1

Motivation

1.1 Field produceable logic

The digital revolution is postulated to go way beyond "personal computation" to "personal fabrication". Based on the above hypothesis, an alternate model of Information and Communication Technology for Development was suggested in [30] with the deployment of FabLabs around the world. The basic notion is to recognize the fact that deployment of tools and skills is necessary for problem solving in developing communities. Thus a set of tools were approximated to perform the function of a"personal fabricator", which would eventually be able to print logic, sensing and actuation on a single substrate. The above model of FabLabs is envisioned to be self replicating cause the equipment should be able to build all the components necessary for making one of its own self.

The challenges in being able to print logic by a desktop manufacturing setup are described. First and foremost, precise control of material properties of printed materials is extremely difficult. This is by far the largest challenge faced by printed electronics community. Crystalline substrates (mostly Silicon and its Oxides, Silicon Nitride, Gallium Arsenide and so on) used in microelectronics industry are highly ordered materials. Organic and inorganic printed transistors require specific organic molecules or nano particle based inks which are difficult to synthesize. Any desktop manufacturing techniques currently can not deposit materials with such order. Also

critical feature size for the components should be small enough that we can integrated a fairly complex circuit on a reasonable sized substrate. Thus rather than depending on the nonlinearities inherently present in the materials, we explore the possibility of geometrically induced nonlinearities. Similar idea was used in fluidic logic proposed in the 60's at high reynolds number flow. This thesis formulates a microfluidic bubble based two phase logic scheme at low Reynolds Number. Thus the logic is implemented with minimum energy surfaces defined by a set geometry in a microfluidic channel. The proposed bubble based logic gates take advantages of the dynamic interface in a two phase flow in microfluidic channels.

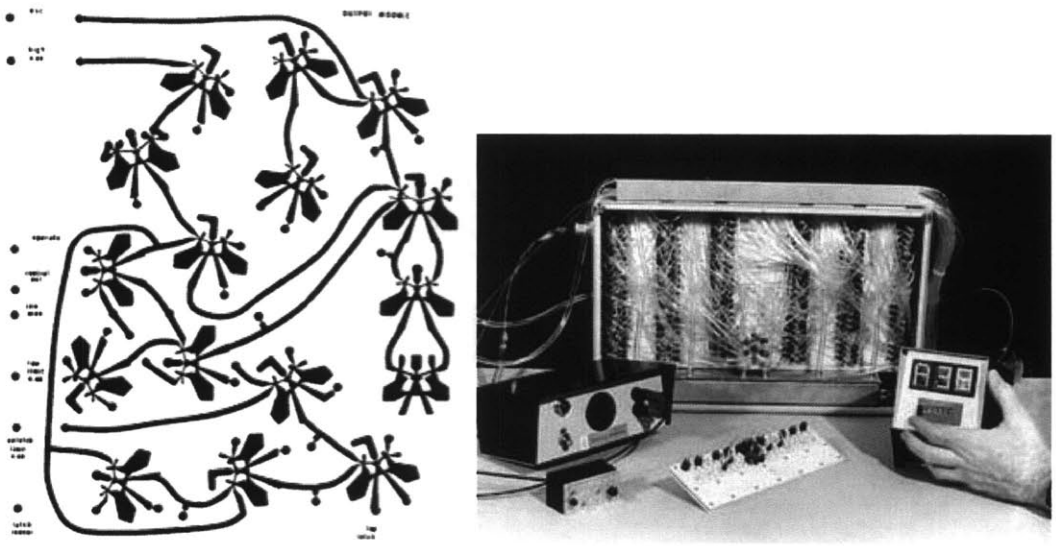

Figure 1-1: (a)A high Reynolds Number fluidic integrated-circuit designed and fabricated at Sandia Labs. Devices similar to the one shown above, rely on non-linear inertial properties of fluid dynamics like jet-jet interaction or coanda effect. At low Reynolds Number inertial terms are dominated by viscous forces which renders inertial effects useless. Thus a simple scaling of devices, as shown above will not work at micron-scales. In literature this is also described as "challenge of low Reynolds Number logic". (b) Fluidic amplifier with a fluidic numeric indicator and an air pulse generator. (image from Natural Museum of American History, Smithsonian)

1.2 Droplet based microfluidic systems

Emulsions in macro world are usually non-homogenous with large array of droplet sizes dispersed in a continuos liquid medium. In a microfluidic system, precise micro-emulsions can be formed via various shearing forces. Many device geometries have been proposed for merging and splitting for such droplets in microfluidic systems. Due to enhanced mixing effects, controlled reaction volume and no diffusion outside of miniature droplet based reaction vessel,[22] such droplet based microfluidic systems are ideal for implementing programmable reaction networks. Benefits of droplet based microfluidic systems have been demonstrated in various systems. [47] used nL sized aqueous droplets to screen hundreds of crystallization conditions using 4nL of protein solution for each trial.

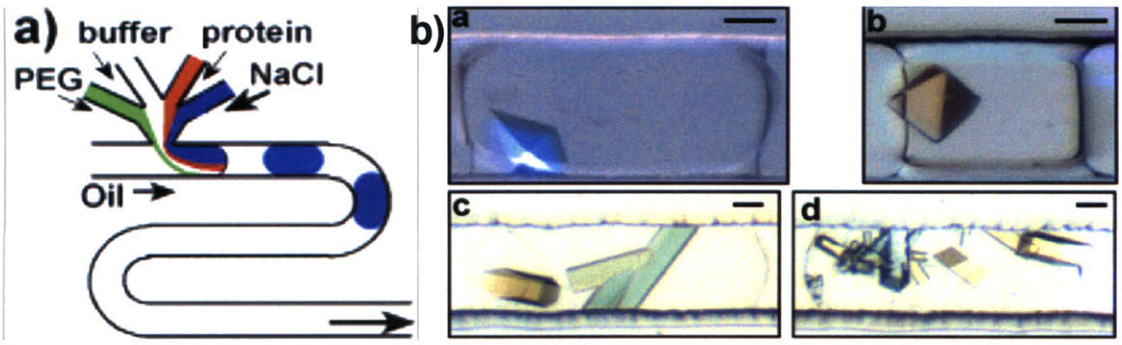

Figure 1-2: Application of droplet based microfluidic system for screening protein crystallization conditions. Image from [47]. a) shows the microfluidic device used for protein crystallization screening. The concentration of various components is varied in different droplets to study different chemical conditions.b) Light micrographs of protein crystals formed inside droplets on a microfluidics chip.

1.2.1 Control system for droplet based microfluidic systems

Effective and flexible control systems play an extremely important role in scalable microfluidic systems.[37] This is clear from extensive use of multi-layer soft lithography based embedded valves reported in numerous microfluidic applications. Though droplet based microfluidic systems have numerous advantages over traditional mi-

crofluidic systems, they still lack a scalable control strategy for manipulating droplets inside microchannels. Two strategies currently employed for manipulating droplets in microchannels can be categorized as active and passive [25] control. Active control [35] [13] of droplet based systems employes a dense micro-electrode arrays with programmed electric field which create dielectrophoretic and electrowetting forces used to manipulate these droplets. With the rising complexity of fluidic devices, such a control becomes fairly complex. Also since the droplets are forced to move on a surface, some benefits which are obtained from purely liquid suspended emulsions are lost (due to surface droplet interactions). Passive control [25] of droplets can be used to merge, split [5] and sort droplets based on local geometries. Such a system lacks the programability and flexibility which exists in micro-electrode based control systems.

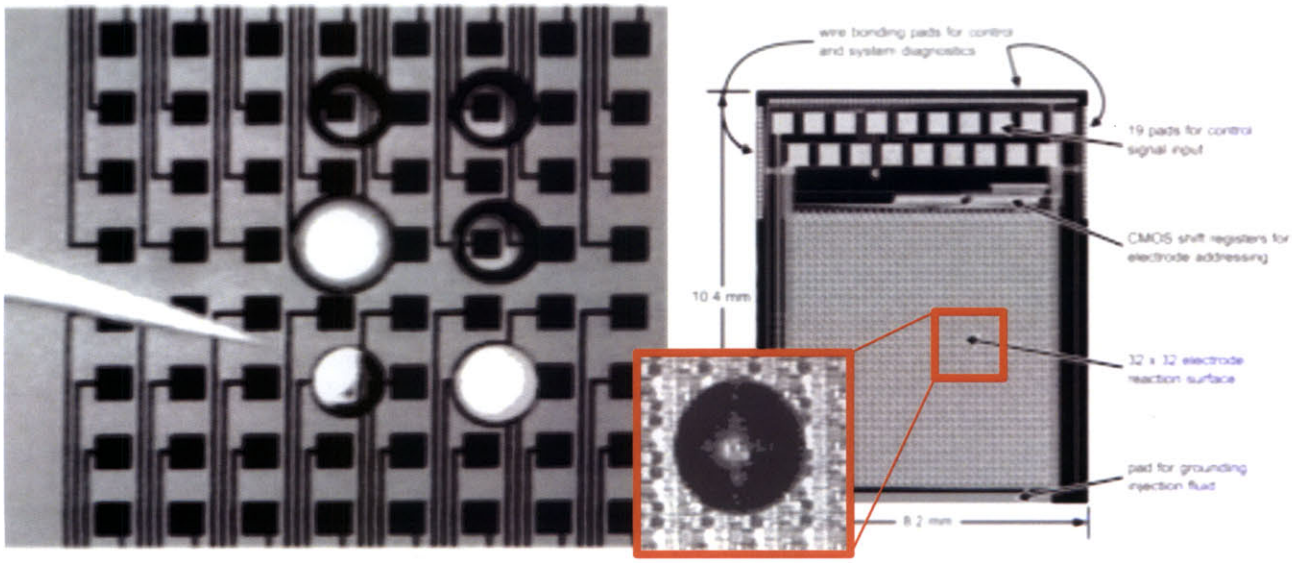

Figure 1-3: Active control of a droplet based microfluidic system. Image from [13]. Figure (a) shows a 100 μm by 100 μm array of electrodes with aqueous droplets. (b) A monolithic SOI CMOS chip as a reaction surface with an array of 32 x 32 electrode array and driving circuit. The chip is an example of a flexible control mechanism for droplet based microfluidic systems. With an increase in complexity of microfluidic reactions complex driving control circuits and strategies are required. An inset shows a 540 μm diameter droplet with 200 μm pitch of the driving electrodes.

This thesis proposes an all-fluidic active control scheme for droplet based microflu-

idic systems. Though current reported work uses a gas-liquid system for experimental evaluations, the control devices can be directly used in a droplet based (oil-water) systems. As compared to a constant pressure driven flow, a pulsating pressure field (analogous to microprocessor clock) is used to drive bubbles in microfluidic shift registers. This provides a precise temporal and spatial control which is obtained only in micro-electrode array based droplet systems. Rather than passive control elements based solely on geometry, this thesis proposes bubble bubble interaction as a control mechanism. For example, a bubble in one channel can control the path or motion of another bubble. The principle of "path of least resistance" ; which implies a bubble takes a path which has a least interfacial energy barrier, is utilized to design various control gate geometries.

1.3 Micro-mechanical logic

The first logic elements were used for mechanical calculating machines. Since than, there has been a tremendous advance in technologies which are used for implementing basic logic elements. Some of them include silicon based integrated circuit technology, organic and molecular transistors, inorganic printed transistors and so on. All of them have an application space which is appropriate for the particular technology. The idea behind a feasibility study of applications of mechanical logic is not to find a replacement to the above technologies. Instead it is to see if there are other applications which might be appropriate to such an implementation. Some of them might include logic elements which are unaffected by strong electromagnetic radiations or computing elements which need a much larger range of operational temperature range which is one of the requirements for robotic shuttles for space explorations.

We broadly define mechanical logic as devices which employ nonlinearities in classical mechanics of the medium to build logic. We categorize mechanical switches (of the kind used in mechanical computing machines), fluidic logic and acoustic logic under this category. Fluidic logic is a promising candidate since it employes no moving parts for its function.

1.4 What can we achieve with a given number of transistors

Here we try to question; what is practically achievable with different implementations of mechanical logic; thus addressing some scaling issues for proposed logic devices.

Consider the following back of the envelope calculation. Consider a manufacturing process which can place transistors with a pitch of say 100 μm. Thus we could place $O(10^2)$ transistors in a row $1cm$ long; with a device density of $O(10^4)$ ie. 10K transistors per cm^2. With better process technology and multilayer processing technology this could be eventually increased. Though nowhere close to what can be achieved by current technologies in integrated circuit design, the number is still promising. In figure 1-4 we plot increasing number of transistor count with the functionalities that have been achieved by the devices. The hypothetical device comes very close to very popular an 8 bit micro-controllers employed in a large number of day today circuitry. Though we realize transistor count is not the only factor that determines the functional complexity, it is still a close approximate. Clearly there are a large set of functions which such high density mechanical logic units could be employed for.

1.5 Outline of the thesis

A general outline of all the chapters is provided in this section. In the next chapter we review basic fundamentals of computation and necessary and sufficient conditions to implement universal computation. A review of magnetic bubbles, their propagation mechanisms, bubble mobility and similarity with bubble/droplet based microfluidic systems is presented. The next chapter introduces the concept of bubble based microfluidic logic gates. Various non-linear devices are designed and fabricated. The notion of bubble shift register, bistable memory and pulsed driving pressure field is introduced. Three techniques for microfluidic device characterization are covered, namely micro-mechanical milling, SU8 based photo lithography and excimer laser micro-machining. A machining process for boro-silicate glass has been developed,

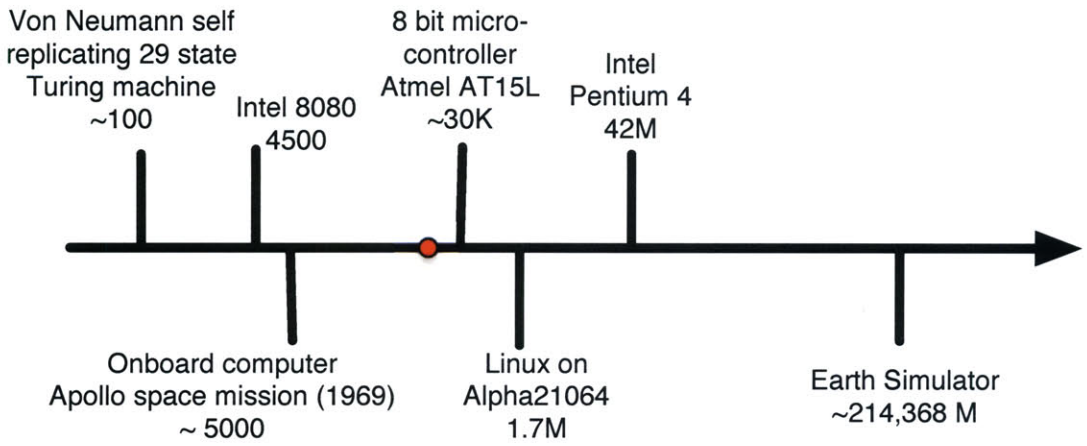

Figure 1-4: What can we accomplish with a given number of switches? Comparing transistor count to Order of complexity achieved in functionality in various devices. The red dot depicts a device with 10K transistors with a pitch of 100 μm in a $1cm$ by $1cm$ area. Thus as is clear from the figure, this gets us very close to current micro-controller used for simple control applications (X axis not to scale)

and devices characterized on a confocal microscope. The last chapter covers the results and future work to come.

Chapter 2

Fundamentals of computation

> "To some, a computer is a physical device in a real world. But being a computer is something that we externally impose on an object. There might be a lot of computers out there, and I suspect there are" Adleman 1994 [1]

2.1 Introduction

There are numerous ways to describe computation. Computation can be based on governing physical laws and mechanisms involved in execution (classical vs. quantum physics), numerous ways of representing information symbolically in the system (analog vs. digital) or/and an architecture for information processing (Von Neumann architecture). A given piece of RNA manipulates information encoded in symbols of nucleotides to compute a protein structure necessary to perform a specific task. A series of mechanical bar linkages interconnected and precisely adjusted in such a way to solve a pre defined partial differential equation, gives you a result by cranking on a lever. A chemical wave propagating in a geometrically constrained excitable media (as demonstrated in a Belousov-Zhabotinsky membrane system) to solve a complex labyrinth. All of the above are examples of computers. Thus a computer could simply be defined as a device with an ability to store and manipulate symbols (depicting information) to generate an output state. These symbols can be abstracted

in various forms depending on the system a computation is being implemented in.

2.2 Imposing computation on physical systems

A large section of this thesis deals with looking for nonlinearities in physical systems that can be casted into a framework of computation. Thus we briefly overview the underlying requirements for a physical phenomena to be useful for computation. To design digital computer based on a physical system, we should be

- Able to represent binary symbols (Unary are not enough). Using a binary system, any piece of information could be represented, thus there is no essential need to go beyond two symbols.
- Able to manipulate these symbols one at a time. A Binary logic gate does exactly that.
- Connect such logic gates together using a notion of wiring.

The above list [36] maps nicely to the turing machine description given by Alan Turing which defines a universal Turing machine. A universal turing machine needs an infinitely long tape (storage) and a read and write head to manipulate the symbols (finite state automata)

2.3 Physical requirements of a computing element

2.3.1 Bit representation

Digital information is encoded in a binary representation of 0 and 1. For different implementations of a computing device, they vary greatly. Here we consider what particles have been used to depict as a bit in classical computers. Starting with the well known electrons, photons [6], magnetic domain [31], protons [42] , ions [17], chemical waves [39] [3] and so on. All these particles are associated with a transport

media which they use for manipulating information, with an energy cost associated with each.

2.3.2 Nonlinearity

Computing elements are inherently non-linear. Devices that process information in a linear fashion can not be assembled together to form a general purpose computer. The property of being able to control an output state based on another input state, leads to the complexity that can be represented only using cascaded non-linear elements. Thus a universal logic element needs to have a non-linear transfer function. Seth Lloyd [28] showed a single non-linear element with linear elements is sufficient for universal computation. Consider a well behaved non-linear function $f(x)$. [28] showed with a set of linear functions including addition and multiplying by a fixed constant and $f(x)$ all universal logic gates could be constructed.

2.3.3 Bandwidth

Band width is defined by inertia of the switching element. It is determined by the time to complete a single switching. The bandwidth of the logic gate in term determines the fastest data rate that can be processed by the element under consideration. It is usually limited by the energy considerations in the transport medium used.

2.3.4 Gain

There are inherent losses that occur in a cascade of elements. These unwanted losses are compensated by gain elements which amplify the input signal to produce an output signal.

Chapter 3

Flow control

3.1 Introduction

Flow control has been an active discipline since the conception of fluid dynamics. [7] Be it the flight of a fly, or drag on the body of a swimming shark; structure of flow plays a key role in determining forces and fields experienced by the object of interest. To be able to structure these flow pattern, various flow control techniques are used by nature. From drag reduction to boundary layer separation to enhanced mixing; fluid flow control has played an immense role in application of fluid dynamics to engineering systems. With the advent of devices with critical dimensions in microns, a new challenge of fluid flow control in this domain has emerged.

Due to a completely different domain of low-reynolds number flow, most of the control strategies applied in high-reynolds number flow are rendered useless. Thus new approaches to flow control need to be developed to bring advantages of flow at small scales to practical applications in the industry and lab-on chip devices.

3.2 Dimensionless numbers

Dimensionless numbers link physical systems to a pure number without any physical units. It is known from Buckingham π-theorem of *dimensional analysis*, the functional dependence between a certain number of variables can be reduced by the number of

independent dimensions occurring to provide a set of independent dimensionless numbers. Such number introduce a concept of scale invariance, thus for a experimentalist the physical regime described in a system is the same for the same dimensionless number. Thus systems can be scaled up and down if dimensionless numbers are the same. Fluid dynamics uses a set of dimensionless numbers to describe flow regimes. We review a set of dimensionless numbers used in the course of this thesis.

- Reynolds number is defined as ratio of inertial forces to viscous forces providing a criteria for dynamic similarity (two flows in the same geometry and Reynolds Number are similar)

$$R_e = \frac{\text{inertial forces}}{\text{viscous forces}} = \frac{UL}{\nu} \tag{3.1}$$

  where U is mean fluid velocity, L is characteristic length and ν is kinematic fluid viscosity.

- Bond Number is a measure of surface tension force to gravitational force given by.

$$B_0 = \frac{\text{gravitational force}}{\text{surface tension force}} = \frac{\rho g L^2}{\sigma} \tag{3.2}$$

  where, L is the characteristic length, g is gravitational acceleration, ρ is density of the fluid and σ is the surface tension, energy per unit area.

- Capillary number evaluates the effect of viscous and surface tension forces at an interface of two immiscible fluids. It is given by

$$C_a = \frac{\text{viscous forces}}{\text{surface tension forces}} = \frac{\mu U}{\sigma} \tag{3.3}$$

  where μ is fluid viscosity, U is mean fluid velocity and σ is interface surface tension.

- Stokes number is the ratio between capillary number and Bond number, which measures the ratio of viscous force and gravity force.

$$S_t = \frac{\text{viscous forces}}{\text{gravitational forces}} = \frac{\mu U}{\rho g L^2} \tag{3.4}$$

3.3 Flow control at high reynolds number

Non-linear inertial effects allow for very effective flow switching in fluidic devices at high Reynolds (R_e) numbers. The technique has been used in a variety of applications for flow control. No-moving parts, high operating frequency and immunity to temperature variations made these devices a very popular control strategy in the 1960's. The two basics mechanisms employed for high R_e control are fluid jet-deflection and jet-wall attachment ("coanda effect").

	Re	Programmability	Flow control eg.
* Surface Tension	independent	surface energy patterning; D. Bebee et al.	Passive capillary valves and control
Boundary layer separation	Re > O(100)	Structure of the channel	Drag reduction using active control
Electro-hydro dynamic instabilities	Re < O(10)	High V electrodes integrated in microchannels	Electro kineatic chips
* Two phase flow	independent	device structure	None
Inertial forces	high;Re >O(500)	flow interaction	Diodes, triodes, amplifiers, gates centrifugal force "lab on CD"
Wall attachment	Re > O(100)	flow interaction	bistable amplifiers

Figure 3-1: Different forces can be used in various settings to control fluid flow. The above table lists relevant forces in fluid dynamics, their dependence on Reynolds number with any examples of use as a flow control technique.

3.4 Challenge of low reynolds number flow control

The fluidic devices discussed in 3.3 work at a typical reynolds number of $O(10^3)$. Smallest device geometries fabricated are roughly of the order of a millimeter. The

physics of these high reynolds number devices starts to break down as channel dimensions are pushed smaller and smaller, since extremely higher pressures are required.

Consider a liquid volume of dimension l, with s velocity gradient of w/l where w is the velocity of the top surface relative to bottom surface. Thus the shear stress is given roughly by $\tau \sim \nu w/Vl$ and the viscous force is proportional to $\nu wl/V$, where V depicts the volume of the fluid cell, ν is kinematic viscosity. The inertial force for the cell would be of the order of l^2w^2/V. Thus reynolds number defined as ratio of inertial to viscous forces is given by wl/ν, denoted as Re. Thus with shrinking dimensions, where l is characteristic dimension, usually low reynolds number Re is observed. For invariance in flow phenomena for different devices, the Reynolds number for the two devices must match. This is intractable for small devices as achieving high reynolds number is extremely difficult. This is significant because most of the devices proposed in the past based on inertial effects can not be scaled down to micron sizes. Thus the inertial physical effects used by these devices (like jet inertial interaction, coanda effect) are not applicable to small geometries. Gain in such devices is defined as ratio of output pressure to control pressure. It is observed that the gain falls sharply after the device is operated in the regime of Re number below 10. Thus new schemes need to be identified for flow control at small length scales.

This thesis proposes to solve the problem of low Reynolds number flow control by looking carefully at all the flow phenomena that dominate flow fields in the regime (figure 3-1). Bubble clogging in microchannels is a common problem in microfluidics. This work exploits the problem to work to our advantage, by designing flow geometries which can precisely control bubble/droplet flow in microfluidic channels.

3.5 Review of current techniques in flow control

Microfluidics allows generation and control of fluid flow in micron sized geometries. The heart of the problem in controlling fluid at small length scales lies in inertial effects becoming insignificant as compared to viscous forces in a microfluidic flow. A table lists all the different physical effects used in flow control in microfluidics 3-1. The

two most common flow regimes in microfluidics are 'couette flow' with a linear flow profile and 'poiseuille flow' with a parabolic flow profile. Inertial and gravitational effects are ignored for this flow regime. In figure 3-1 we mark out surface tension effects and two phase flow as promising control strategies.

The driving forces are either applied at inlet/outlet or generated locally by specific effects. The importance of certain phenomena is specific to the flow-regime and is dependent on R_e number of operation. Thus effects which are crucial in working of devices at macro-scales are rendered useless if scaled geometrically cause of a completely different flow regime in operation for scaled down devices.

3.5.1 Typical operating conditions in a micro-channel

For a $100\mu m$ channel with water (shear viscosity of $\eta = 0.01gm/cmsec$) with a $1cm/sec$ flow rate amounts to a R_e number of unity. Even with substantially higher flow velocities, the Re number remains in the laminar regime, well below laminar to turbulent transition ($\sim$ 2000). Since streamlines in laminar flow do not cross each other, mixing happens only due to diffusion in straight channels. Various external forces can be applied to the fluid flow. For a fluid cell inside a micro-channel, its behavior can be affected by inertial, viscous, capillary, gravitational, electro-kinetic, magnetic, frictional and static forces. The relative magnitude of the above listed forces varies tremendously with change in flow regimes.

Since the conception of idea of a Lab-on-chip devices, a large number of flow control mechanisms have been proposed in the literature [19] [41] [37] [29] [43]. Disadvantages of the listed systems include very large scale scalability and complexity in fabrication. Here we briefly review applications of multi-layer soft-lithography for fabricating monolithic valves and pumps.

3.5.2 Monolithic PDMS valves and pumps

An extension to soft-lithography, multi layer soft lithography was proposed in [41]. Devices with multiple layers from soft materials can be fabricated using this technique.

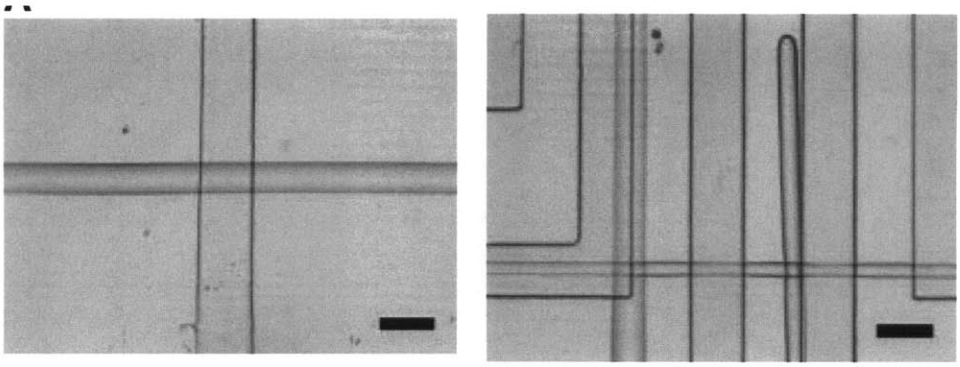

Figure 3-2: Several devices from [41] are shown(200μm scale bar). (a) A simple two layer elastomeric valve (B) A multilayer elastomeric device produced by stacking thin elastomeric layers on top of each other.

It also made possible to build integrated pumps and valves in these multi-layer devices thus opening up a new paradigm in integrated microfluidic systems. The technology lies at the heart of various microfluidic devices which were previously not possible cause of complex integrated control system necessary for operation. This later led to large scale fluidic integration of components [37] , which is very similar to what happened in the semiconductor industry with the advent of large scale monolithic integration techniques.

The most basic device which can be formed using multi layer soft lithography is a two layer valve, which is formed by intersecting two fluid lines in a cross pattern (as in figure 3-2). The top layer is defined as a control layer while the bottom layer carries the fluid of interest. The control fluid used is high pressure air which acts on the fluid layer to switch the flow on-off as desired. The key implementation hurdle for such devices is precise alignment of multiple fluidic layers while bonding. This is done using alignment jigs with a clear optical axis to align the two PDMS parts which are bought together to form the device. The footprint of a single valve can be fairly small thus making large scale integration possible. This is a promising technique for integrating a large number of active valves in a microfluidic device for complex flow control problems.

Another control device that is made possible by multi-layer soft lithography is an elastomeric pumps. Elastomeric peristaltic pump are two layer devices (3D model

as shown in figure 3.5.2) They work by actuating air pressure patterns which are implemented by turning specific valve "open" and "close". The pumps are frequency of operation dependent with maximum flow rate of 2.5nL/sec for a pump with 100μm wide and 10μm high channels. Thus these pumps can be implemented in a very small footprint on a PDMS based soft lithography chip for nominal flow rates.

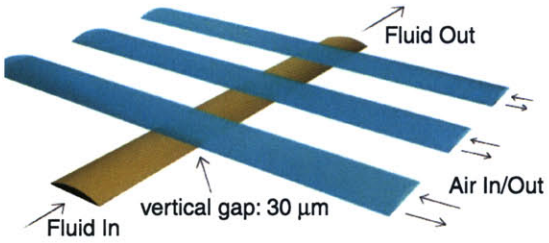

Figure 3-3: Basic operation of a elastomeric peristaltic pump.

The need of complex control systems for microfluidic systems is clearly indicated by a long list of applications which were made possible by above described integrated PDMS valves and pumps. The following figures list several of these applications

An integrated monolithic PDMS valve and pump based architecture for control has been used in a wide array of applications, mainly focused around bio-moleculer seperation, amplification and detection. Following is the list of lab on chip applications monolithic PDMS valves have been used

- Real time Polymerase Chain Reaction (PCR), which is an amplification reaction for DNA molecules [27]
- 2D protein separation [44]
- Active pH control
- On-chip protein crystallization [16]

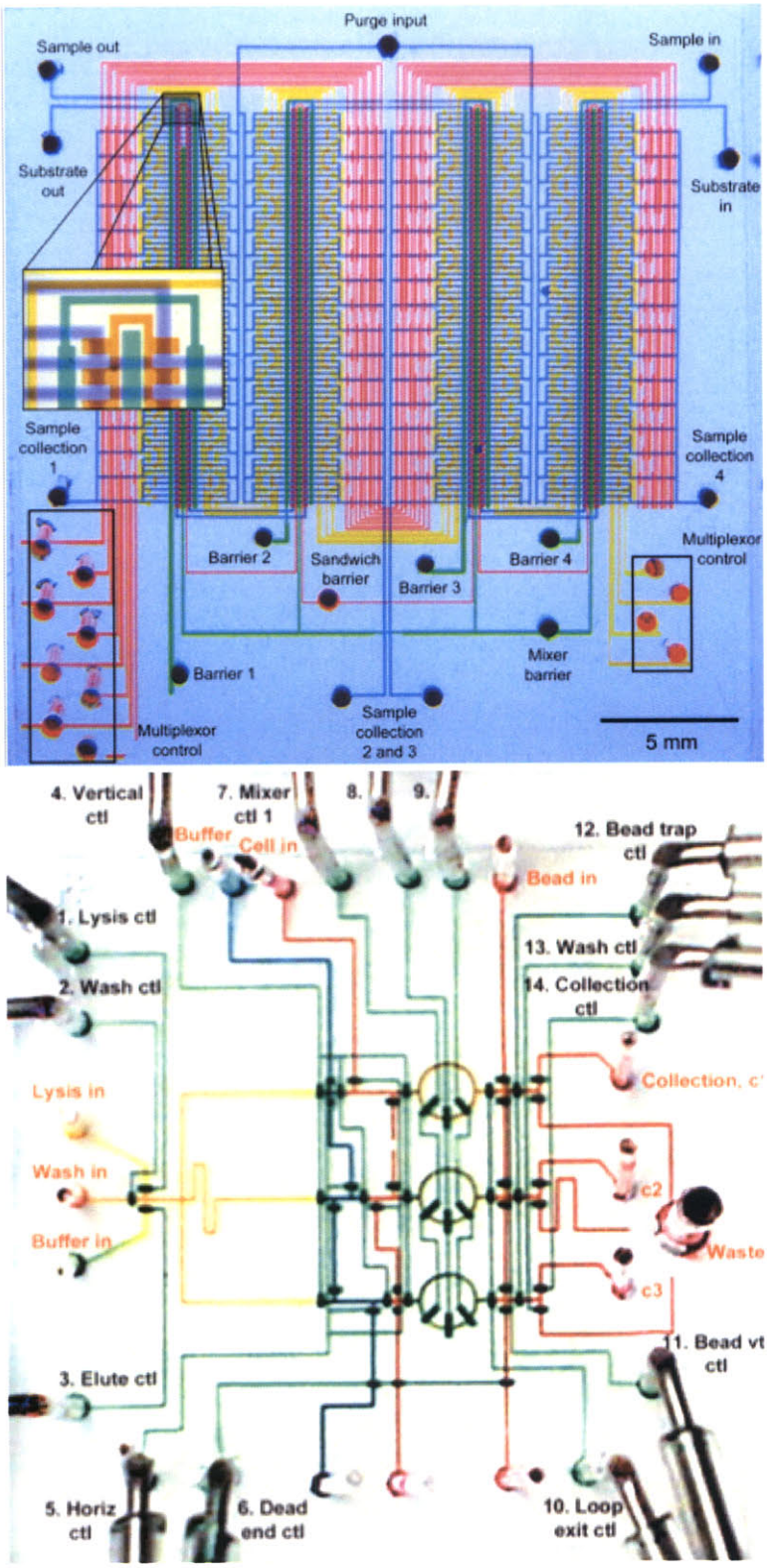

Figure 3-4: A list of applications made possible by integration and flow control techniques at small scales. (a) A high throughput system for screening flourescence-based single-cell assays from [19] (b) DNA purification chip. from [20]. Lysis on live bacterial cells can be performed and DNA fragments obtained in 3 parallel channels.

3.6 Active flow control in"dead wood"

This section looks at natural system that evolved a flow control strategy for maintaining transport capacity of the system. Almost two-thirds of the total water that is transported from land based water bodies to the atmosphere passes through microfluidic networks inside trees and plants. A typical tree might expend 400 liters of water per day, circulating though its body with a hydraulic system with no moving parts [18]. Such a large scale movement of water from roots to leaves almost entirely flows in spaces not bounded by a cell membrane, that is "dead wood"[48]. Thus maintaining the flow capacity of such a system is very crucial for survival of plants. "Air seeding" or bubble nucleation in extremely long microfluidic channels can very easily disrupt capillary force based flow responsible for mass transport in a plant. pH mediated changes in hydraulic resistance of a tree stem has proved existence of active hydrogel (pectins) based control scheme for plants to regulate their internal flow regime. [18] Shrinkage and expansion of this pectin matrix is thought to change flow dimensions of micro-channels which in turn control flow properties of the channels.

Chapter 4

Magnetic Bubbles

4.1 Introduction

This thesis proposes use of air bubbles as a low reynolds number implementation of a all fluid no moving parts logic gate. As discussed in previous chapter, implementation of a information processing system requires the ability to create, manipulate, interact and destroy bits of information. With the advent of microfluidic systems and better understanding of two phase flow it is now possible to manipulate individual bubbles in confined geometries. Thus we look at how can do information processing in such a system.

A similar scheme for information storage and processing was proposed in the 70's called magnetic bubble technology. Several memory chips were introduced in the market to replace expensive memory devices at that time. A review of the technology and various devices implemented for its close analogy to air bubble logic is presented.

Magnetic bubbles are cylindrical domains of reversed magnetization in a thin film of magnetic material. Magnetic bubbles can exist as an isolated state or interact with other bubbles to form arrays, lattices and other interesting patterns. Bubble-bubble interaction lies at the core of magnetic bubble logic implementations. For magnetization to define a bubble, the film must have a preferential magnetization perpendicular to the film as compared in plane magnetization. For a magnetization of $4\pi M_s$, the additional energy is given by $2\pi M_s^2$. To prevent the collapse of the

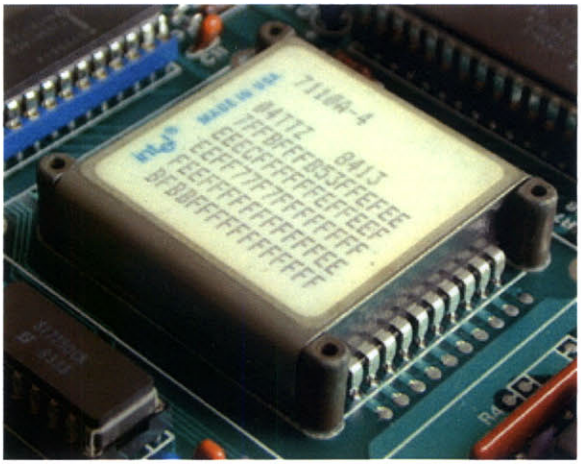

Figure 4-1: Intel's 1 Megabit magnetic bubble memory, the 7110 was introduced in 1979. With the introduction of larger hard disk systems in the early 1980s, all work on bubble memory stopped which pretty much killed bubble memory entirely. (Image courtesy Memory Components Handbook Supplement 1984)

bubble, the material must posses uniaxial magnetization isotropy K_u. The ratio $\frac{K_u}{2\pi M_s^2}$ is defined as Q (clearly for a material to support bubbles $Q > 1$). The film supports magnetization patterns which provide flux closure on a fine scale, without an external field. [8] An example lattice structure is shown in figure 4.1.

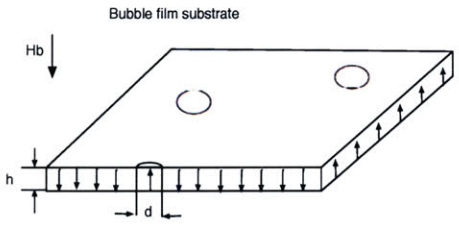

Figure 4-2: Individual magnetic bubble in a thin magnetic film

Without any external magnetic field, the unmagnetised state of the film contains equal domains both facing upwards and downwards. Application of a external magnetic field H_b grows one magnetization at the expense of the other. Magnetised materials tend to rotate the plane of polarization of an electromagnetic radiation via its interaction with electrons in the material. Thus using polaroids magnetic bubbles can be seen as shown in figure 4.1

In this chapter we will cover the basic introductory physics of magnetic bubbles. Various devices for creation, annihilation, propagation and manipulation in

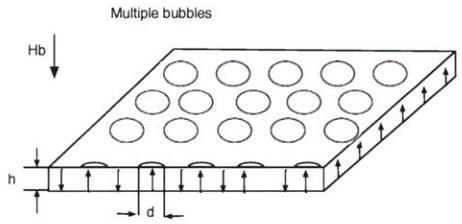

Figure 4-3: Multiple magnetic bubble in a thin magnetic film forming a regular lattice.

Permalloy-Bar technology will be discussed. Various implementation schemes for creating bubble logic will be discussed in light of producing similar devices in two phase mono disperse air bubbles. The device implementation for magnetic domain provides design guideline for replicating the system in two phase fluid domain. In the last section the inherent analogy between air bubbles and magnetic bubbles will be discussed.

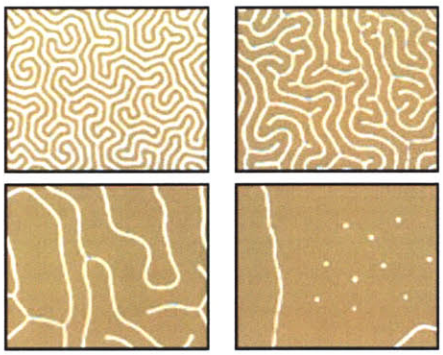

Figure 4-4: 100X magnification photomicrograph with 0H sat., 0.77H sat., 0.95H sat. and 0.99H sat. Equal magnetic domains are seen when no bias field is applied, while only individual magnetic bubbles exist at 0.99H sat.

4.2 Dynamics of Magnetic Bubbles

An external bias magnetic field H_b oriented parallel to the magnetization outside the bubble on a magnetic thin film is necessary to stabalize magnetic bubbles. Two little bias field and the bubbles will explode into strip lines (called stripout), while two much bias field can cause the bubbles to collapse. Variation in H_b cause the bubble size to vary as shown in figure 4.2 Thus with $Q > 1$ and bias field H_b in

appropriate range, magnetic bubbles are stable. [8] In this section we will review dynamic properties and various devices used for controlled bubble propagation.

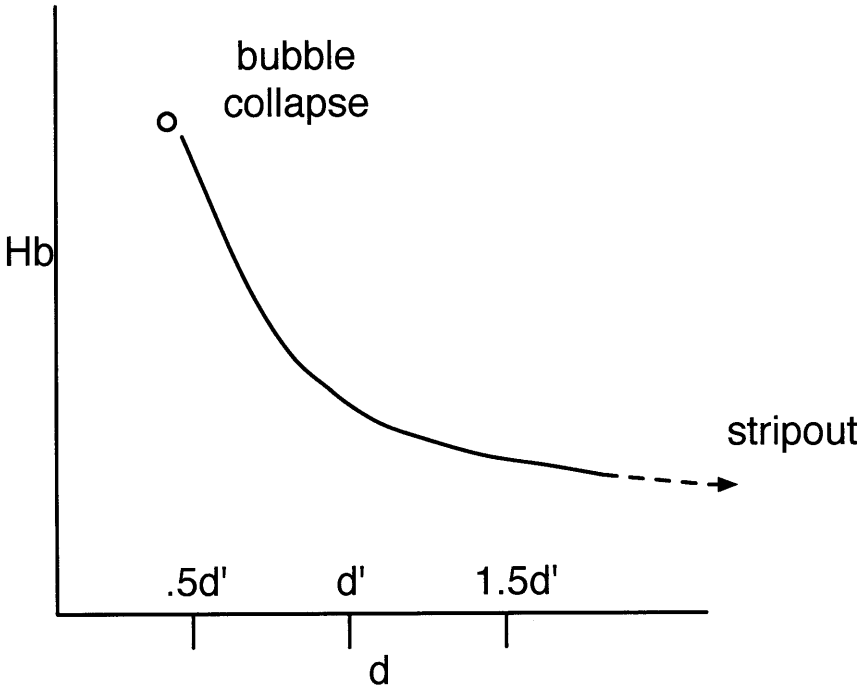

Figure 4-5: Bias field vs. bubble size

4.2.1 Equilibrium configuration of an isolated bubble

Consider a magnetic bubble in state of static equilibrium. The static configuration of the bubble is defined by an associated total energy and characteristic bubble dimension, d/h where h is thickness of the magnetic film and d is the diameter of magnetic bubble. The configuration is dependent on film properties and magnetic environment. In this section we will summarize the magnitude of energies associated with an isolated magnetic bubble and dependence of magnetic environment to the bubble size without deriving them. A good reference for the derivations is [8]

To obtain total energy associated with a single isolated bubble, we will list all the contributing energy densities and integrate them over bubble volume (V). The energy contributions come from the wall energy density integrated over domain wall

area E_W, and volume integral of magnetostatic energy density E_M and magnetic field energy density E_H.

$$E_T = E_W + E_M + E_H \tag{4.1}$$

where all of them and evaluated to be the difference between bubble present and bubble absent.

The reversal of magnetic domains inside the magnetic bubble does not occur abruptly. This is because neighboring spins tend to keep each other aligned in the same direction. Thus the transition region associated with a bubble is termed as the bubble domain wall (δ_W). A larger δ_W ie. smoother domain transition, increases the anisotropy energy density E_K. Anisotropy energy density is related to preferred orientation of magnetization with respect to internal structure of the film. . Thus total wall energy for a circular bubble of diameter d and film thickness h is given by

$$E_W = \sigma_w(\pi dh) \tag{4.2}$$

$$\sigma_w = 4(AK_u)^{1/2} \tag{4.3}$$

where A is exchange energy constant and K_u being unaxial anisotropy parameter.

For a circular bubble, E_M is the magnetostatic energy density. With no external field E_M should be approximated by $-2\pi M_s^2 V$ where V is averaged volume where reversed spins provide flux closure. For a very small d/h, V approaches $\pi d^2 h$. For a larger bubble, V is approximated by $2\pi dh^2$. Then for a reasonably large bubble

$$E_M \simeq -2\pi M_s^2 \cdot 2\pi dh^2 = -2\pi M_s^2 (d/h) 2\pi h^3 \tag{4.4}$$

Stability in the system is introduced with an external magnetic field H_B. Associated magnetic field energy density is given by

$$E_H = 2M_s H_B \pi (d/2)^2 h \tag{4.5}$$

Thus E_H is quadratic in dimension of the bubble d while it scales linearly with applied

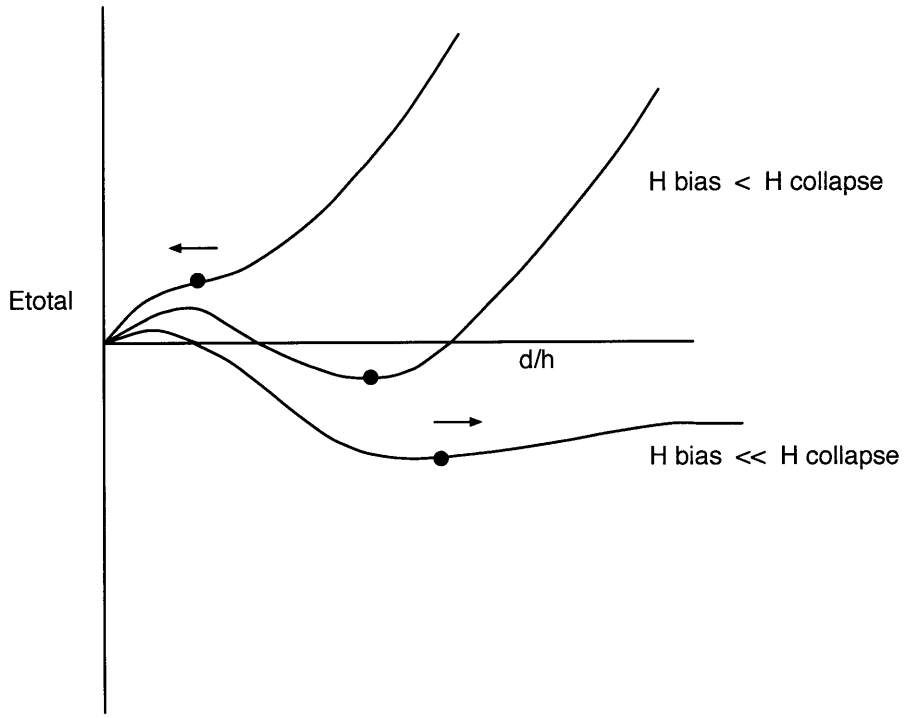

Figure 4-6: Total energy associated with individual magnetic bubble vs. d/h. The minimum occurs at d_0. The bubble collapses if bias field is greater than H collapse.

field H_B. Finally we can plot E_T with respect to d/h. The minimum occurs at d_0 as indicated in figure 4.2.2.

4.2.2 Bubble mobility

In the last section we established a relationship of bias field to mean diameter of an individual bubble. With an increase in bias field H_B, each segment of the bubble wall moves outwards. The tension in the wall segment increases. The effect changes the diameter but causes no net bubble movement. Simple equation of motion of bubble is established in [8]. For a gradient in bias field, ∇H_B velocity of the bubble is given by

$$V = -\mu_B(\triangle H_B - \frac{8}{\pi}H_c) \tag{4.6}$$

where

$$\mu_B = \frac{\mu_w}{2}, \triangle H_B = d \cdot \frac{dH_B}{dy} \tag{4.7}$$

where bubble mobility is half of wall mobility.

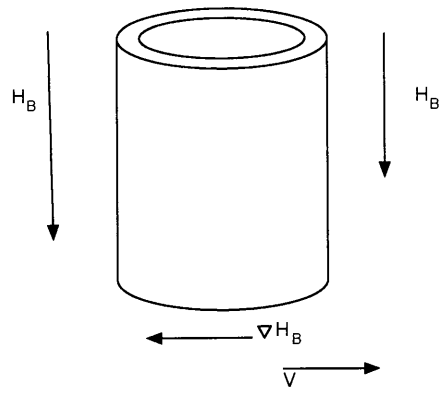

Figure 4-7: Field gradient applied on a cylindrical bubble. The gradient causes the bubble to deflect in opposite direction with a velocity given by V. With a constant increase of bias magnetic field H_B (as discussed in previous section), each segment of bubble wall moves outwards but no net movement of bubble occurs.

4.2.3 How are magnetic bubbles manipulated?

If information is represented as presence of magnetic bubbles, they would need to be created, manipulated and destroyed.

Bubbles are propelled by creating a gradient in the bias field. Because of a gradient in the bias field, the bubble moves to a region with lower bias field. This minimizes the magnetic energy of the system. The gradient field can be created in various ways, with conducting current wire. Propagation along a fixed track is achieved by coupling a rotating in-plane field to a track of permalloy bars in various shapes. Thus the geometry of the permalloy bars creates a magnetic energy landscape. The bubble moves to the minima of this energy landscape. Propulsion can be achieved by applying another in-plane field which modifies the energy landscape.

The speed of propagation for magnetic bubbles depends on dynamic properties of the bubbles, as well as the magnitude and frequency of rotating field.

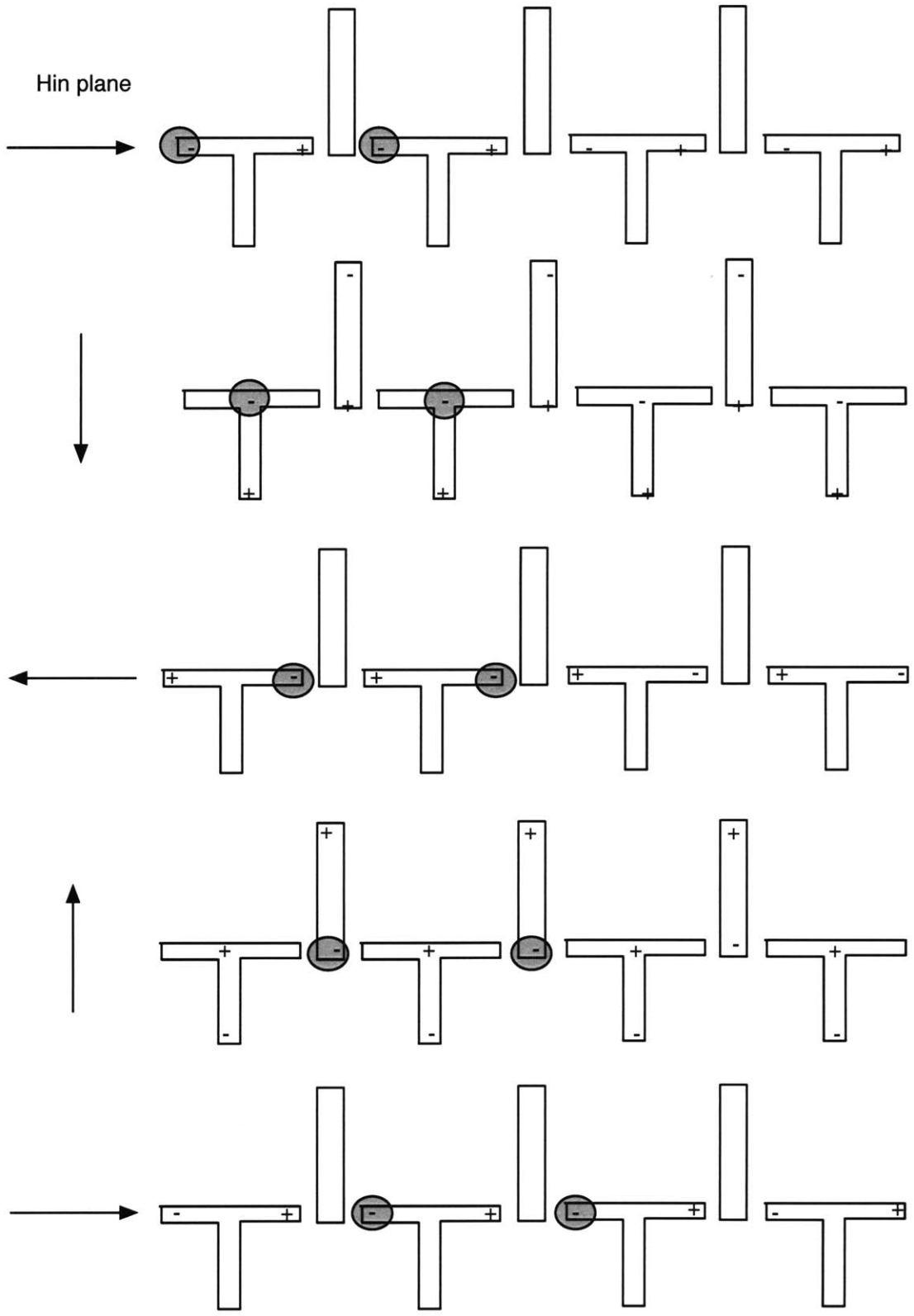

Figure 4-8: Propagation sequence with rotating magnetic in-plane field. The magnetic bubble travels from left to right, in a single rotating cycle of in-plane field (H_ip)

4.3 Analogies between magnetic bubble and air bubble logic

The following figure 4.3 summarizes the similarities in transport properties and physical dynamics between magnetic bubbles in thin magnetic films and air bubbles in confined micro-channel geometries. .

Similarity between magnetic bubbles in garnet films and perm-alloy layers and air bubbles confined in micro-channel geometries.

Magnetic Bubbles	**Air Bubbles**
Discontinuity in magnetic (vector) field	Discontinuity in pressure (scalar) field
Manipulation by gradient in bias field	Manipulation by gradient in pressure
Driving rotating field provides periodicity	Driving pulsating pressure provides periodicity
Bubble momentum is unimportant	Bubble momentum is unimportant
Directed in confined paths using perm-alloy geometries	Directed in well defined microchannels
Production, replication, annihilation, splitting possible	Production, replication, annihilation, splitting possible

Figure 4-9: Table summarizing the similarities between magnetic bubbles in garnet films confined by perm-alloy patterns and air bubbles in confined microfluidic channels.

Chapter 5

Microfluidic bubble-based logic gates

5.1 Introduction

As described in section 3.4 new physical principles need to be used for being able to do no-moving part fluidic logic at small scale. In this section bubble based microfluidic logic gate and devices are proposed. The system can also be implemented using droplets in immiscible liquids. For the proposed device an air-water based two phase flow system is used. The non-linerity exploited in such a scheme is the dynamic interface shape for two immiscible liquids. Since the liquid bubble tries to minimize the interface energy of a liquid gas system, certain energy minima exist for the bubble in a defined geometry. The energy landscape can be changed by applying pressure of inducing flow, thus manipulating the bubbles to a new location.

This chapter reviews the physics of bubbles confined in small channels. Many different phenomena interplay roles in fluid dynamics of two phase flow. For a bubble based system being described, surface tension, surface properties of the solid, contact angle hysteresis etc are important. Next two kinds of logic devices are proposed which differ in bit representation. The bit representations used for the devices are either location of a bubble or pressure signal at a specific location. Though the two family of devices can be used together in a single device, we define them separately in order

to simplify the description.

5.2 Surface tension

Effect of surface and interfacial tension is known to give rise to many diverse phenomena in day to day life, including soap bubbles in a bath tub, capillary rise in narrow tubes, shape of a rain drop and so on. Interfacial phenomena can be studied in various ways including geometrical, molecular simulation etc. Assume the average intermolecular force applied on a molecule in a liquid is same in all directions, called the mean field approximation. At an interface of a gas-liquid system the argument fails since the intermolecular force on a molecule in a liquid is far much larger than on a molecule in the gas phase. Thus liquid molecules are being attracted inwards and sideways but there is no balancing force in opposite direction. Thus the surface behaves like a membrane under tension.

Making an energy argument, energy of a surface molecule is higher as compared to one inside the liquid. Thus Thus surface of liquid interface contracts to minimize this energy. For force per unit length contracting the surface

$$\sigma = \frac{\partial F}{\partial A} \tag{5.1}$$

where *sigma* defines the surface tension of the liquid. Surface tension of liquid vapor interface at 20 degC for water is $72.88 mNm^{-1}$ whereas for mercury it is $486.5 mNm^{-1}$.

Considering curved interfaces (since the contracting forces have a tendency to curve an interface), pressure deferential across the interface can be described using the famous *Young-Laplace equation.*

$$\triangle p = \sigma(\frac{1}{R_1} + \frac{1}{R_2}) \tag{5.2}$$

where R_1 and R_2 are radii of curvature of the surface along orthogonal tangents and $\triangle p$ is the pressure difference. For a spherical case describing bubbles and droplets,

where R_1, R_2 are equal to r

$$\triangle p = p_i - p_e = \frac{2\sigma}{r} \tag{5.3}$$

Thus pressure difference across a plane interface is zero.

Arguments similar to fluid-fluid interface can be applied to studying liquid-solid interface (with solid interface being immobile). Thus consider a drop of liquid on a solid surface. The liquid either wets the surface completely or forms a defined region which is wetted by the liquid. For the later case, if θ defines the contact angle at the line of contact for the liquid drop

$$\sigma \cos\theta = \sigma_s g - \sigma_s l \tag{5.4}$$

the above equation is called Young's equation where $\sigma_s g$ and $\sigma_s l$ are surface tensions associated with solid-gas and solid-liquid interface. The above equation is valid only when the droplet is in quasi static equilibrium. If there exists a flow field where the contact lines are moving (as is the case with bubbles inside microfluidic channels) a concept of dynamic contact angle is defined. The above equation is no longer valid for a moving contact line, cause the angle is also a function of speed of the contact line with respect to the solid substrate. [34]

5.3 Capillary motion

Motion governed by forces associated with surface tension is termed as capillary motion. For a curved interface between two immiscible fluids, the pressure difference is given by the *Young's Laplace* equation. Since the normal stress needs to be balanced at the interface, an equal hydrostatic pressure balances the pressure differential in case of a rising liquid in a capillary tube. For a capillary tube inserted in a liquid, the meniscus which is approximately hemispherical with constant radius of curvature r given by

$$r = \frac{a}{\cos\theta} \tag{5.5}$$

where a is the radius of the capillary tube. The criteria of hemisphericity can be given as

$$h \ll (\frac{\sigma}{\rho g})^{1/2} \tag{5.6}$$

which is also defined a s capillary length. Also the equilibrium height the liquid column will attain is given by

$$H_0 = 2(\frac{\sigma}{\rho g})\frac{\cos\theta}{a} \tag{5.7}$$

The ratio of viscous and surface tension forces is defined as capillary number, another dimensional number useful in identifying the operating region of a given problem. Thus

$$Ca = \frac{\text{viscous force}}{\text{surface tension force}} = \frac{\mu U}{\sigma} \tag{5.8}$$

where U is characteristic velocity.

5.4 Physics of bubbles in micro geometries

Bubbles in a microfluidic system are generally an annoyance which has to be worked around. Thus a microfluidic engineer tries to work in a regime where no bubbles are produced due to the flow. This work takes advantage of the pressure differential that exists inside a vapor bubble. This is used to build simple logic gates as described in following sections.

5.4.1 Motion of a bubble in capillary tube

Consider slow motion of an air bubble of length L inside a capillary tube of radius a. A front and a rear menisci exist which are shaped differently. For small capillary numbers, surface tension forces dominate the viscous forces. Here gravitational forces will be ignored. An experimental observation [34] that volume of flow rate of liquid swept out by the bubble moving with speed of the air-liquid interface relative to the wall must equal the average speed of the liquid in front of it, $-V$ multiplied by the

cross sectional area of the tube. Applying conservation of mass

$$UA_{film} - (-V + U)A_{tube} = 0 \tag{5.9}$$

$$\frac{V}{U} = \frac{A_{tube} - A_{film}}{A_{tube}} = \frac{A_{bubble}}{A_{tube}} \tag{5.10}$$

The speed with which the bubble exceeds the average speed of the liquid in the tube is $U - V$, also denoted as UW where W is fractional velocity change.

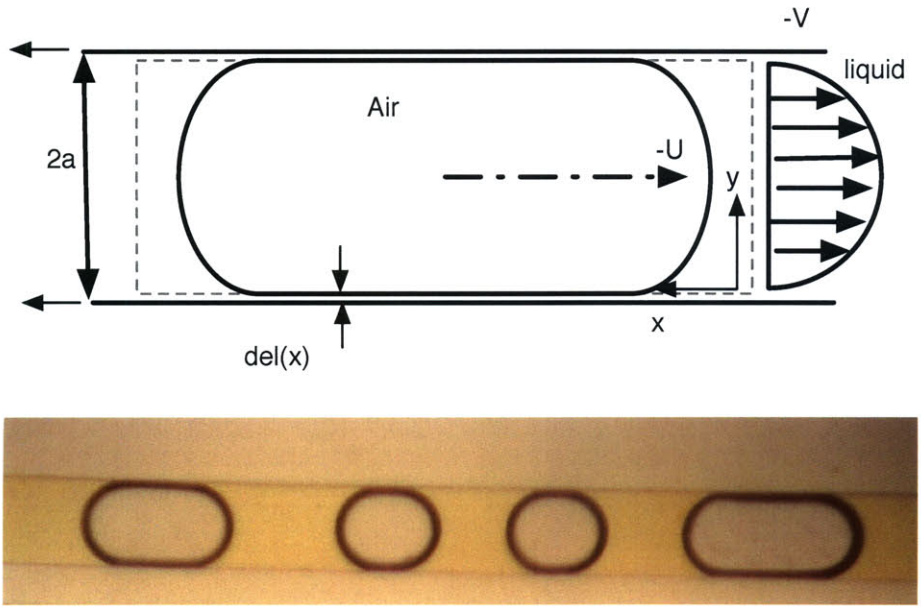

Figure 5-1: (A)An air bubble moving in a circular capillary, with origin fixed with respect to the bubble. A thin film forms around the bubble, very similar to coating flows.(B) Photomicrograph of actual bubbles of different sizes in a 200 micron channel. The stable geometry of the bubble is nearly ideal.

5.4.2 Bubble clogging

Bubble clogging has been studied experimentally. Quasi static analytical model for bubble clogging in microchannels was recently proposed in [24]. The clogging pressure model is briefly described here. In general a bubble clogging model would require modeling of wetting, dynamic contact angle, static and dynamic friction, geometry of the channels, interface between the two fluids in 3D with the fluid dynamics of

bulk fluids. Here only a quasi-static model of incompressible bubble in a symmetric capillary contraction is being reviewed.

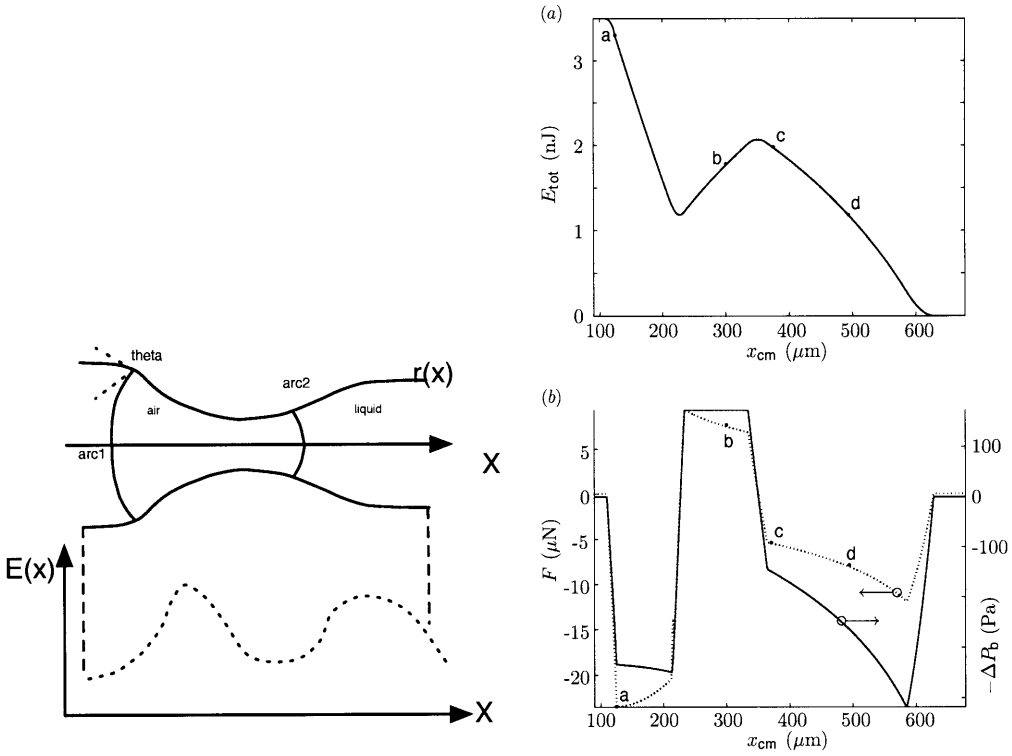

Figure 5-2: (a) Given a geometry defined by $r(x)$ varying along X axis, and symmetric about X axis; energy profile can be calculated along the X axis, where center of mass for the bubble varies along X. The profile varies from geometry to geometry. The partial differential of energy with respect to x_cm gives the force required to balance it. (b) [24] calculates energy and force profile for a bubble traveling in a channel constriction with tapering angle 20 deg. Figure from [24]

A sharp contraction of a channel for a defined geometry offers an energy barrier for a gas bubble to go across. This results in a clogging pressure, maximum pressure needed to push the bubble through the constriction. Since the device geometries we look at are fairly small and flat, we will assume a 2D model where the z axis is ignored and no gravitational effects are accounted for. Thus total energy for a air bubble in a channel can be written as

$$E_{total} = \sigma_{lg} A_{lg} + \sigma_{sg} A_{sg} + \sigma_{sl} A_{sl} \tag{5.11}$$

The total volume of the bubble, $Asgh$ (h being channel height), is conserved and no

compressibility effects are accounted for. Thus for center of mass of the air bubble defined as x_{cm}varying only along X axis (due to symmetry), the force needed to balance the air bubble is defined as

$$F = \frac{dE_{total}}{dx_{cm}} \tag{5.12}$$

Now from the *Young's Laplace equation* 5.2 we can find the geometry of the air bubble given the first contact point for any arbitrary channel geometry. This is using an assumption that channel height h is very small and thus the liquid gas interface is cylindrical with circular arcs, when viewed from top. Thus A_{lg} is given by $(length_{arc1} + length_{arc2})h$. Similarly other areas can be calculated to evaluate the total energy of the system. Now force required to hold the bubble in a quasi-static equilibrium is given by 5.12.

From [24], the clogging pressure for a axisymmetric channel contracting with a tapering angle θ of 20^0 is shown 5.4.2. The maximum force required to push the bubble through determines the clogging pressure for the system.

5.5 Shift registers and propagation geometries

The basic principle of bubble clogging is used to construct a large number of devices. A large number of propagation geometries were considered for this work. Since the force needed to push a bubble through a narrow constriction is dependent on the shape of the constriction, various energy profiles can be obtained. The interface shape tries to minimize the total energy of the bubble, thus forcing it to move to an energy minima.

Every profile (except a in fig: 5.5) has a periodic minima along X axis, where the interface energy for a bubble trapped is minimized. The energy profile (as shown in fig 5.4.2)can be altered by applying a pressure field along X axis, forcing the bubble to move periodically in X direction. Thus a precise time control over the movement is obtained. This also introduces the notion of clocking for microfluidic devices since the

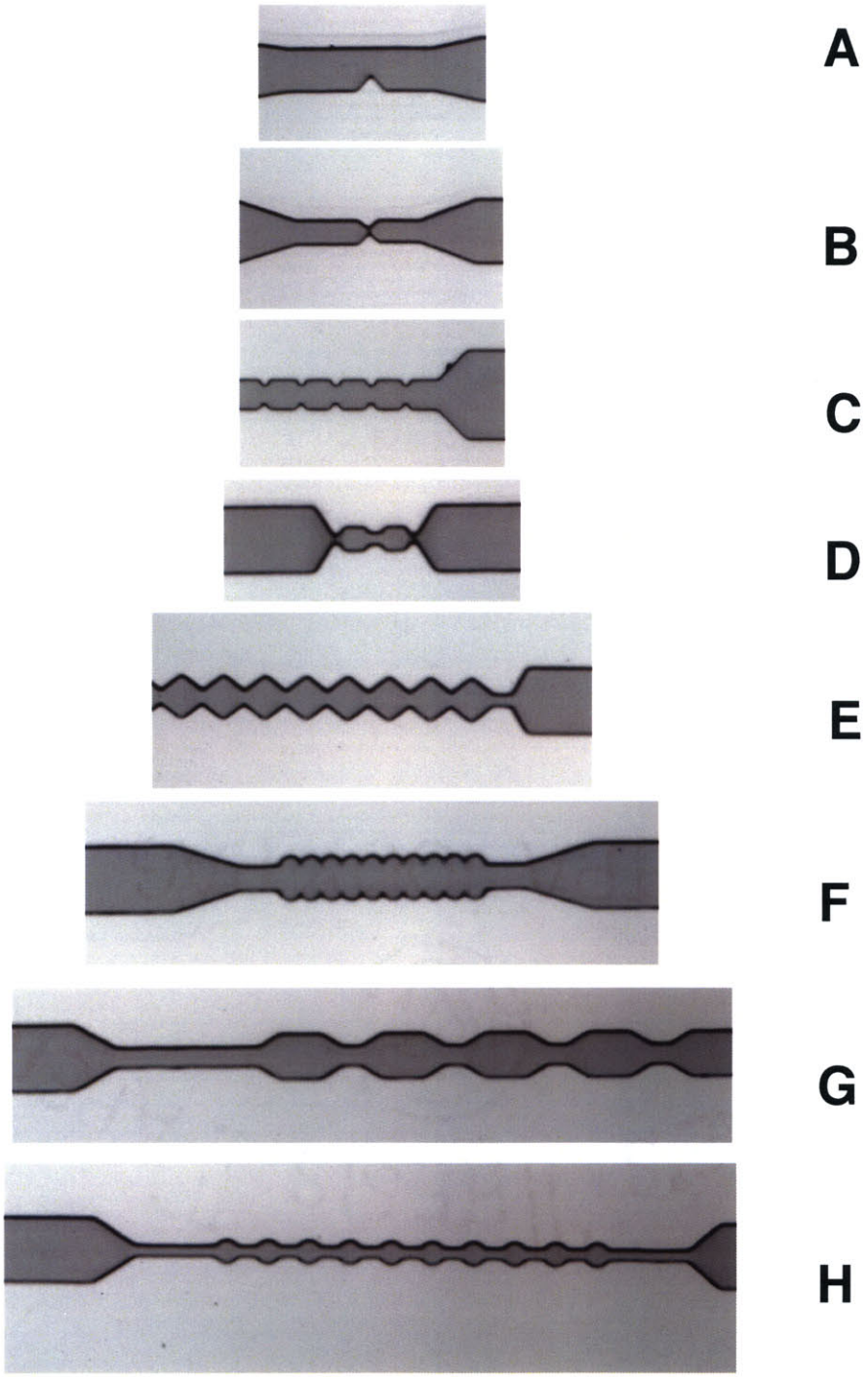

Figure 5-3: Shift registers for bubbles in microfluidic channels. The geometry of the channel wall determines the energy profile along the axis of propagation of the bubble, say X axis. Various profiles from A to H are shown in the figure above. Because of the different geometries they all exhibit different energy profile.

device runs on a fixed pulsating pressure clock. The pulsating pressure is implemented by a simple switching solenoid (Lee valve) being operated at a fixed frequency. This basic principle is used to design an array of shift registers. Since it takes a discrete amount of force to push a bubble through a narrow constriction, a pulsed pressure pulse can be used to move the bubbles in a series of constrictions in sync with each other. This provides a precise time control of bubble movement inside microchannels. In future work, the energy and force profile for shown geometries will be evaluated and compared to clogging pressures experimentally. With more number of bubbles in series, the pressure needed to push them through the series of constrictions increases linearly, due to a pressure differential across every bubble.

5.6 Bistable memory element

Bistability is an important criteria for information processing devices, because it allows for information storage. A simple constriction based bistable bubble device is shown in figure 5.5 (D). The channel consists of two chambers tied together by a narrow channel. The two chambers are further bounded by extremely narrow channels so as to form a energy barrier for the bubble to escape. The clogging pressure argument considered a geometry which when mirrored along the Y axis yields the device being discussed in this section. Thus the energy profile for a bubble in such a geometry is also symmetric with two energy minima when the center of mass of the bubble lies at the center of the two chambers. A threshold pressure moves the bubble from chamber A to chamber B, thus flipping a bit of information. Readout ports are provided at the chamber which makes non-destructive readout of the memory possible. The state can also be optically read from the device itself. the memory is non-volatile since it does not require any external energy for the state to remain stable. A large array of such memory elements could find applications in fluidic displays.

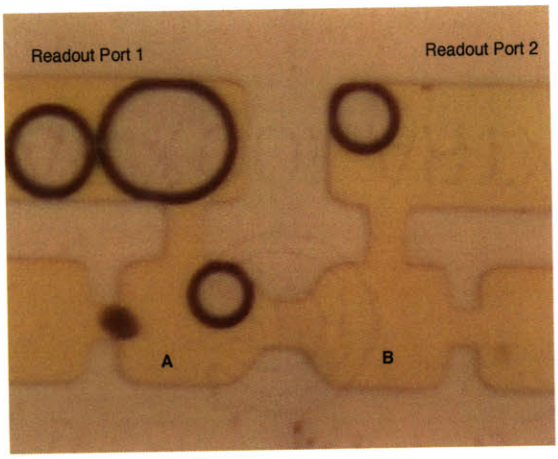

Figure 5-4: A bubble memory with readout ports. Chamber A and B represent bit states (with a bubble present or absent). the device is bistable since both configurations are stable. The transition requires a pressure pulse to move the bubble from one chamber to another. The readout ports can read the pressure in the corresponding chamber, thus providing a mechanism to simultaneously read the memory without destroying it.

5.7 Bubble based embedded pressure sensor

Pressure distribution with specific flow rates varies with constructed geometry inside microchannels. To characterize a device for the pressure loss that occurs due to variations inside a microfluidic channels various pressure sensing schemes have been proposed in the literature. Due to complexity in fabrication of most of the present schemes for pressure sensing, analytical models are more often employed to evaluate resistance of a microfluidic channel.

This thesis proposes a novel pressure sensing scheme in complex microfluidic networks. The pressure measurement is based on size of micro bubbles in a port connecting to the micro-channel. The bubbles do not touch the wall surface and hence are spherical in shape (disregarding gravitation at small length scales). From equation 5.3 we know the difference between external and internal pressure of a air bubble is given by $\frac{2\sigma}{r}$, where r is the radius of the micro bubble and σrefers to the surface tension of air-liquid interface. Hence radius of the bubble is directly correlated to external pressure.

Consider a single bubble in an infinite domain of liquid at rest with a uniform

temperature. The bubble is assumed to maintain spherical symmetry and nearby solid boundaries are ignored. Bubble dynamics with a radius $R(t)$ and external pressure $p_\infty(t)$ at temperature T_∞ is given by *Rayleigh-Plesset equation.* [4] We consider a quasi static case for a bubble radius ignoring all the dynamics involved at the interface. The assumption would be true if the bubble is given sufficient time to evolve and is in equilibrium with the external fluid. Also any compressibility of external liquid is ignored (constant density ρ_L). The viscosity of the liquid is also assumed to be constant (μ_L). The contents of the bubble are assumed to be homogenous and the temperature (T_b) and pressure(P_b) is considered always uniform. Finally the system is assumed to be isothermal and considered to evolve slowly. For a isothermal compression of ideal gas

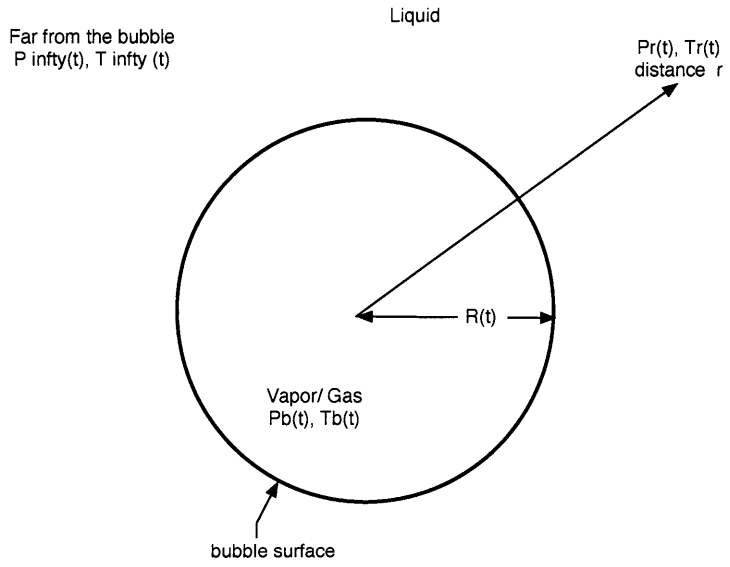

Figure 5-5: Schematic of a spherical bubble in infinite fluid.

$$P_1 V_1 = P_2 V_2 \tag{5.13}$$

Now, when external liquid pressure at $P_\infty(t)$ changes from $P_\infty(t_1)$ to $P_\infty(t_2)$, the internal bubble pressure changes based on the ideal gas law from $P_b(t_1)$ to $P_b(t_2)$.

Also from 5.3 we know that

$$P_b(t_2) = P_\infty(t_2) + \frac{2\sigma_{lg}}{R(t_2)} \tag{5.14}$$

where radius at time t_1 is given by $R(t_1)$. Applying ideal gas law we get

$$\frac{P_b(t_1)}{P_b(t_2)} = \frac{R(t_2)^3}{R(t_1)^3} \tag{5.15}$$

Hence knowing external pressure both at time t_1 and t_2, and bubble radius at time t_1, final bubble radius at time t_2 can be evaluated. For a bubble of $100\mu m$, stable at an external pressure of $10psi$ and surface tension for air liquid interface of $73mJ/m^2$; we can evaluate the change in radius for a rise of external pressure by 10 psi. The new radius for the bubble at $20psi$ should be $79.5\mu m$. This is a considerable change which can be easily detected by various optical techniques.

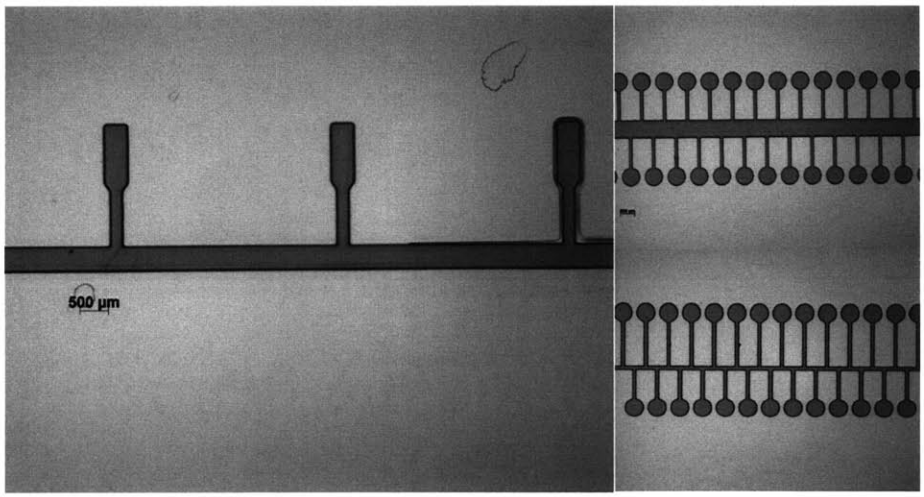

Figure 5-6: Photomicrographs of SU8 molds of pressure sensor. Two designs are shown in above figure. Small bubbles are induced in the channel at a precise location using excimer laser pulses.

The channel geometry in figure 5.7 shows two different port structures which were fabricated. The channel height is close to $100\mu m$. The bubbles are induced using excimer laser pulses in the confined geometry.

5.8 Devices based on bubble-bubble interaction

In this section various devices which rely on bubble bubble interaction for operation and described. Bubble bubble interaction is necessary for designing a non-linear gate. Direct and indirect bubble-bubble interaction phenomena is used in various devices which are proposed. Direct interaction devices are based either on bubble fusion and fission considering change in bubble volume, or for non fusing bubbles (stabilized by a surfactant), by change in air-water interface shape. Indirect interaction is governed by the pressure difference across a bubble. In brief the three principle nonlinear logic devices proposed in this section are

- Path of least resistance based AND/OR gate
- Cross over AND/OR gate
- Bubble fusion fission based AND/OR gate

Different on chip bubble generators are used along with the logic gates. Spatial and temporal control of bubble interaction is obtained by using shift registers (as described in 5.5) as propagating path for the bubble. For example for bubble coalescence, employing shift register like structures ensures a temporal control over the coalescence. All the described devices are driven by a pulsing pressure field, which is equivalent to a clock frequency used in electronic circuits. Thus bubbles in the above logic gates can be driven at a fixed clock frequency.

5.8.1 Path of least resistance based AND/OR gate

Resistance of a bubble contraction can be defined in terms of total free surface energy change when a bubble is moved from a large channel to a narrow channel. Here only surface energy change for the bubble is evaluated, The energy loss due to streamlines converging is currently ignored. Consider a channel traveling from a capillary of radius R to a narrow capillary of radius r. An external pressure P_R and $P_L$is assumed around two bubble interfaces where the total pressure drop across a bubble is given

by $P_L - P_R$. Considering isothermal quasi-static motion of the bubble we can evaluate the surface energy loss to move the bubble from a large to a narrow channel. The change in energy can be described as in [24]

$$\triangle E_{total} = E_1 - E_2 = \sigma_{lg}(A_{lg,1} - A_{lg,2}) + \sigma_{lg}\cos\theta(rl - RL) \tag{5.16}$$

where L and l describe length of the air bubble in large and narrow channel respectively. For a large bubble numerical evaluations show ([24]) that energy is required to push the bubble from large to a narrow geometry. Thus an analogy can be established via defining a resistance associated with narrow constriction. For a series of constrictions, the resistance can be added in parallel, if there exists a bubble in a constriction. We assume this resistance for a air bubble going across a constriction is much larger than the resistance offered by such a constriction to single phase flow.

From above, a simple resistance based model for the proposed AND/OR gate can be constructed. Thus two devices are proposed on the basis of *path of least resistance.* Consider AND/OR gate described in figure 5.8.1. Bubbles from two generators arrive at the intersection, forming A and B stream. Since the driving pressure is pulsed, the motion of bubbles is in sync, with a unitary shift with every time step. Let us consider all the possible cases for bubbles arriving from A and B. Based on the channel geometry, the path for least resistance for A, weather any bubbles are present or not in channel B is towards channel marked A+B. For bubbles in channel B, path for least resistance when no bubbles are present in channel A is also given by A+B. In case the junction is occupied by bubble from channel A, the above statement is no longer true. Thus bubble from B is forced to take path marked by channel A.B . Looking more closely at the geometry of the described junction

$$a < b < c < d \tag{5.17}$$

where a, b, c, d describe the constriction dimensions for the marked channels A.B, B,

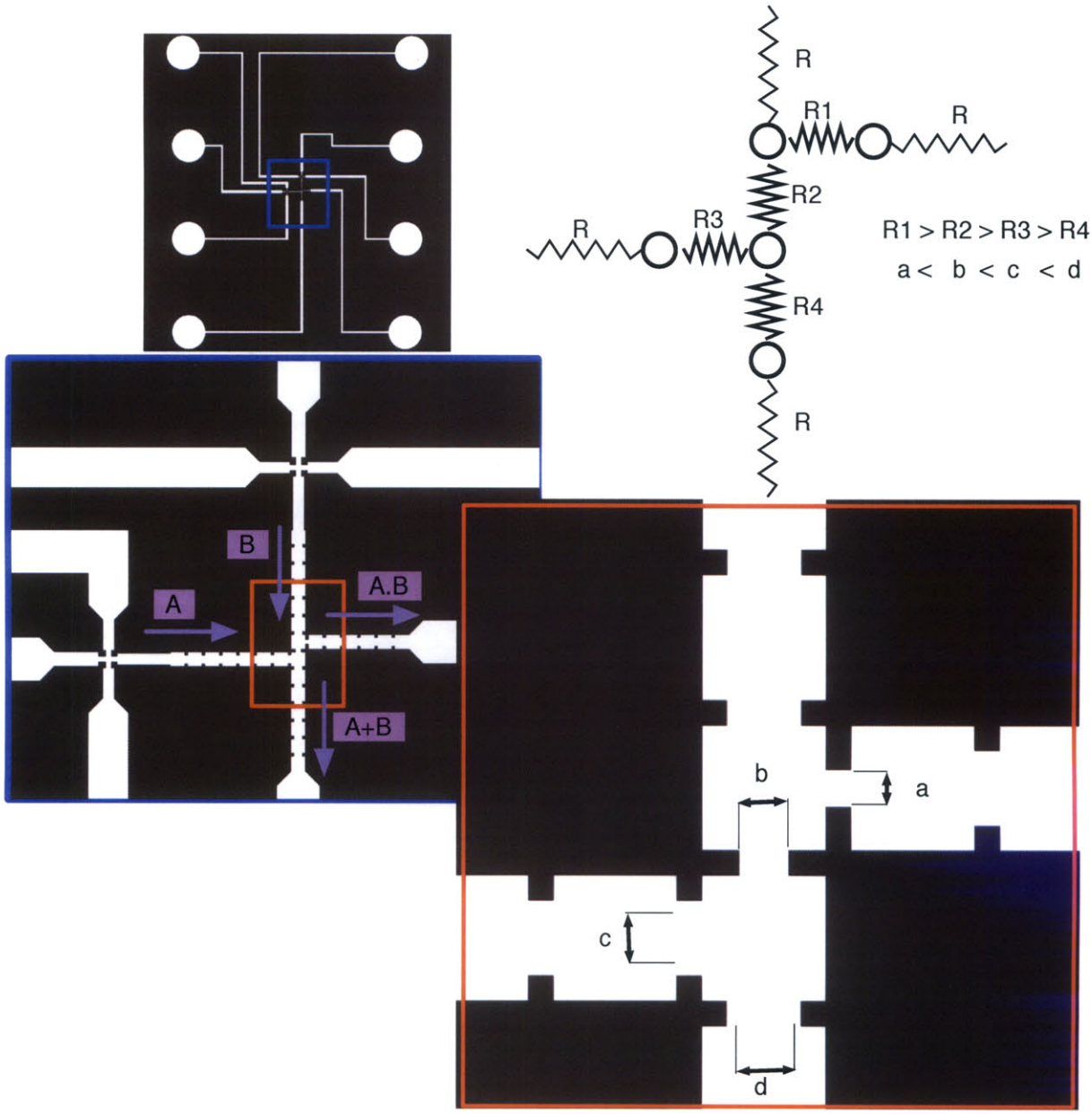

Figure 5-7: Constriction based AND/ OR logic gate. The principle behind the device is based on the fact that air/water interfaces minimize their energy while going through a constriction. Thus a path of least resistance is offered by downward going "A+B". This is the case when either one of A or B is arriving at the junction at an instance of time. If both bubbles arrive at the same time, due to additive nature of pressure drop across a bubble, the second bubble is forced to take the bath towards A.B. A reduced order resistance based model is shown in figure, where the resistance represents the constriction size at a channel. Thus $R1 > R2 > R3 > R4$ and $a < b < c < d$ where a, b, c, d represent the constriction in the channel in the order shown in the figure.

A, and A+B. Looking at a simplified resistance model for the above

$$R_1 > R_2 > R_3 > R_4 \tag{5.18}$$

where R_1, R_2, R_3, R_4 are as depicted in figure 5.8.1. Thus the above geometry provides both AND and OR gate where, A+B depicts an OR gate (a bubble flows to channel A+B, if there exists a bubble in A or B); while A.B depicts a AND gate (a bubble flows to channel A.B only when bubbles are present in both A and B). The fabricated devices with device variations are shown in figure 5.8.1

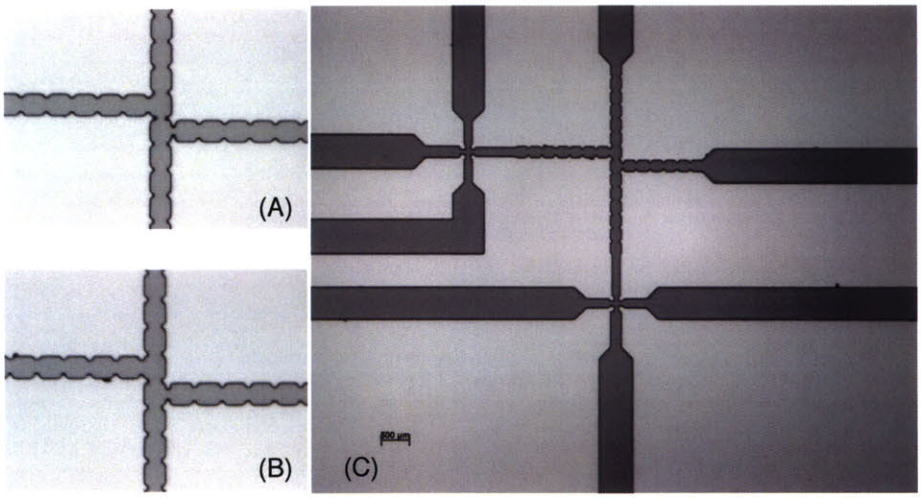

Figure 5-8: Fabricated AND/OR gate described in figure 5.8.1. Two variations in constriction geometries are shown in (A) and (B) while the complete device with bubble generators is shown in figure (C)

Another device based on path of least resistance is described in figure 5.8.1. The device principle is very similar to the previously described gate, though the geometry is based on a lateral interaction of two bubbles in parallel channels. The path of least resistance for a bubble bubble in channel A is marked in figure 5.8.1. Bubble in channel B always propagates to channel marked A+B. In case of a interacting bubble present in channel B at the junction of A and B, bubble in channel A is forced to follow the path to A.B . Thus an AND and an OR gate is implemented in the above device. as in the previous device, both channels A and B are driven by a pulsating

pressure periodic in time. The pressure acts like a driving clock providing control over the interaction of the bubbles. With no driving pressure, bubbles are most stable in enlarged chambers (connected together by narrow constrictions).

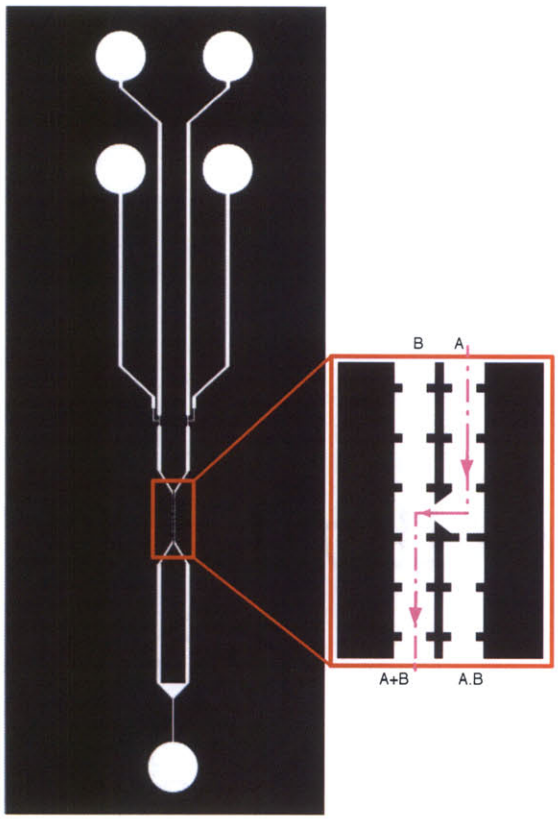

Figure 5-9: Another device based on path of least resistance. AND / OR gate based on bubble interaction in parallel channels. Air bubble present in channel one forces bubble in channel two to flow from a path with larger constriction.

Since the described device has multiple trenches in the defined geometry. Fabrication of large trenches in SU8 based photolithography requires well collimated light sources. In the fabrications runs so far, the device could not be fabricated flawlessly. Changing the illumination light source should be able to get rid of the problem. Fabricated devices with faults and ill defined channels is shown in figure **??**.

5.8.2 Cross junction AND / OR gate

A cross junction AND OR gate is described in this section. The gate is very similar in functionality to billiard ball logic gates proposed for the first time in [10], where

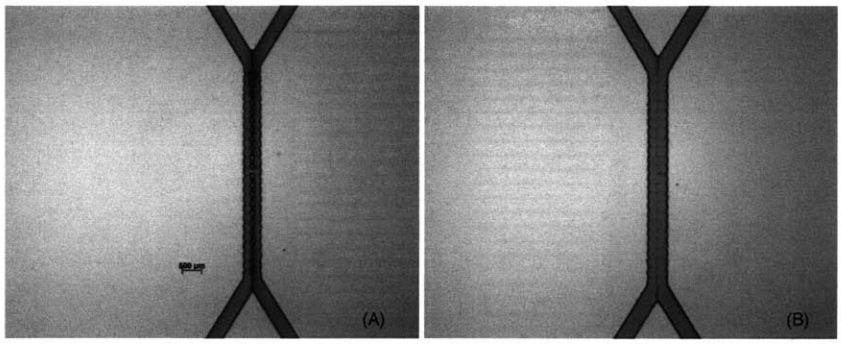

Figure 5-10: AND / OR gate fabricated in SU8 mold. Due to narrow trenches in the design and high aspect ratio required, the yield for the device was very low. A collimated exposure source will help in device fabrication.

notion of conservative logic was introduced. Here non coalescencing bubbles are used as carriers which are repelled at a junction to take different output paths. The bubbles are stabilized by using a very small quantity of a surfactant in the liquid solution. At the junction the constriction size determines the preferred path for the bubble. Various variations in the geometry have been fabricated for the cross junction device.

SU8 mold of the fabricated device with variations in geometry is shown in figure 5.8.2.

5.8.3 Fusion fission based logic device

Fusion and fission of droplets in microfluidic channel has been studied separately. [5] [25] A scheme for AND / OR logic gate is proposed using controlled coalescence and splitting of bubbles. Bubbles arriving from channel A and B are fused together at the junction. The coalescence of the two bubbles results in a larger volume of the resultant bubble. This bubble is further propagated to a splitting geometry where the bubble is split again. Since the size of the splitting region is matched with the total volume of fused bubbles, fission only occurs in the limiting case when two bubbles were joined together in previous step. If a smaller bubble is passed through to the fission geometry, it passes through without splitting towards channel marked as A+B, thus performing an OR operation. When a bubble is split (case when both a and B are present), one of the bubbles is forced to take the channel marked A.B thus

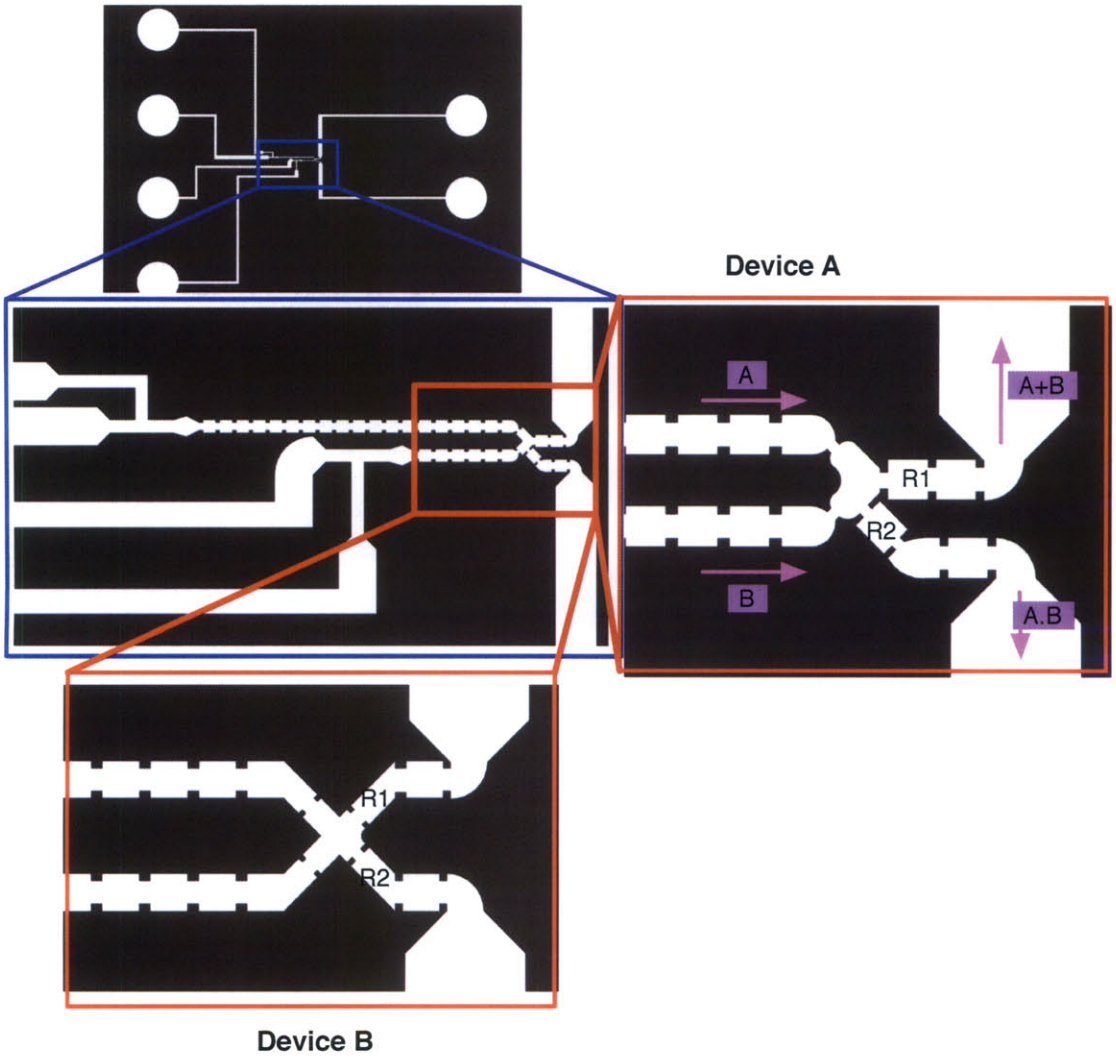

Figure 5-11: Cross over based logic gate. In the figure two devices with the same principle are shown. The constriction for output path is represented by pressure resistance given by $R2$ and $R1$ where $R2 > R1$. A shear based bubble generator is used to generate the bubbles at the first place.

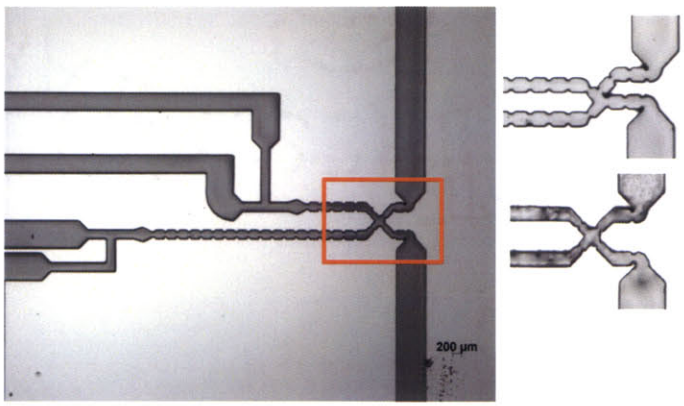

Figure 5-12: Fabricated cross junction gates in SU8. Two junction geometries were used as shown in the insets. The two distinct paths have variation in channel constriction thus preferring one path over the other.

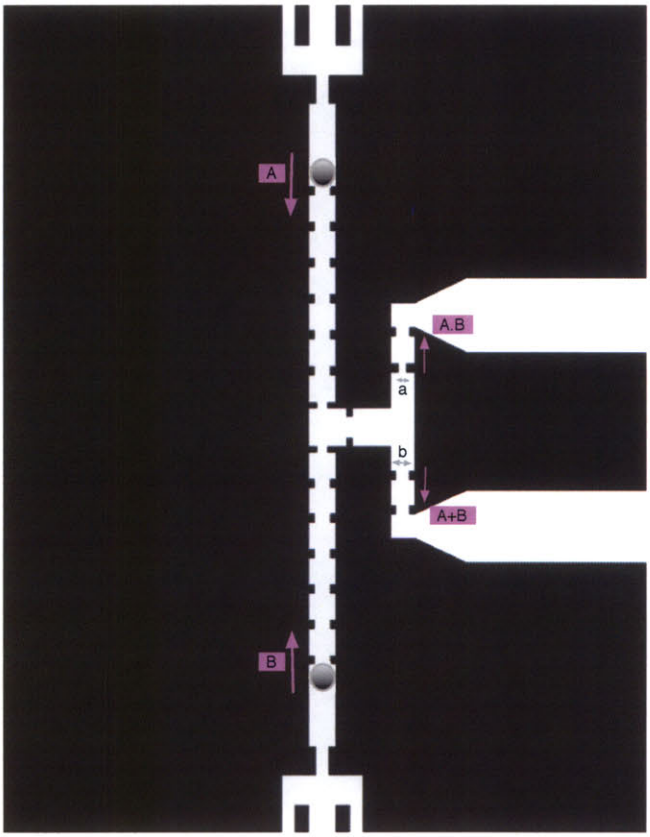

Figure 5-13: AND/OR gate based on fusion and fission of air bubbles (droplets). The bubble splits at the T junction, based on interfacial shear on the bubble. If the bubble radius is less than the maximum dimension of the channel.

performing an AND operation.

Another geometry for bubble splitting is shown in figure 5.8.3. The designed geometry can be used to divide a bubble into two, thus cloning a bit in another sense. Bubble splitting at the junction happens due to shearing flows. It is assumed that the incoming droplet size fills the channel completely.

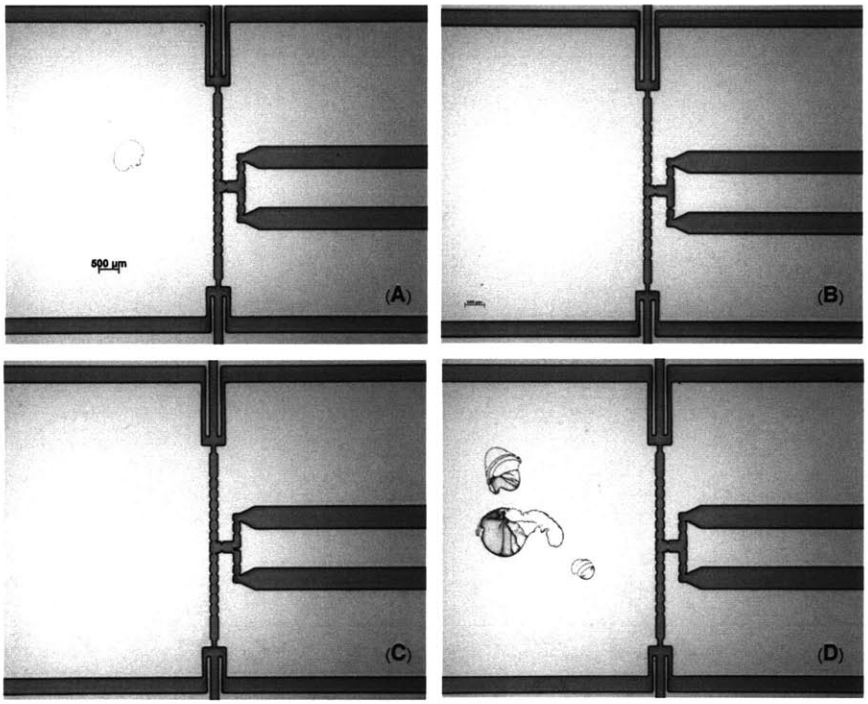

Figure 5-14: SU8 molds of fabricated fusion fission gates. Various device variations in the fission geometry are shown in (A), (B), (C) and (D)

5.9 On-chip bubble generators

Notion of on demand bubble (droplet) formation is still missing in microfluidic devices. An on-demand bubble generator would provide a precise time control for fluidic devices. On demand ink-jet printing provided a huge revolution in control of fluid dispensing and thus opened up a large array of application. A similar concept of a two phase flow based bubble (droplet) generation in a microfluidic device would enable dispensing fluidic bubbles (droplet) as required for a on chip reaction. Various

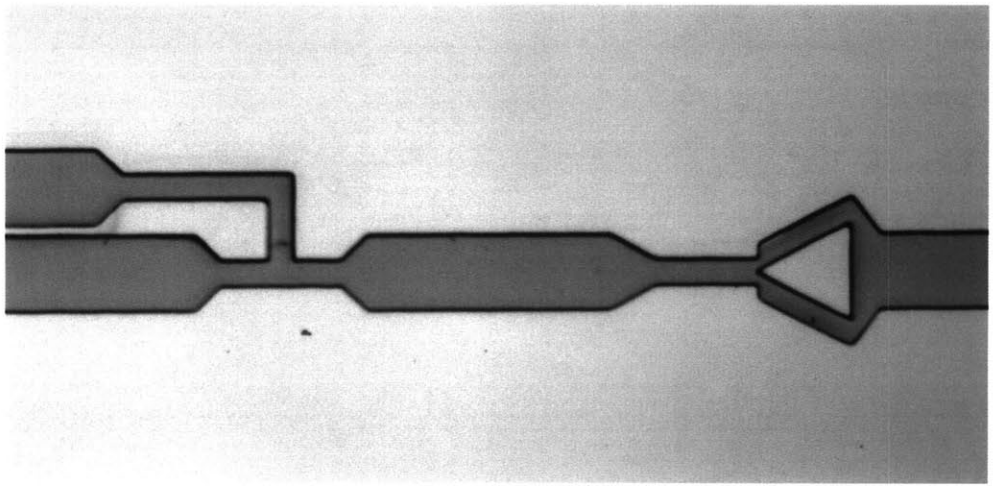

Figure 5-15: Bubble splitting for reproducing information. Incoming bubbles are split into two when they arrive at the junction because of shearing flows.

continuous droplet generators have already been reported in the literature. [38] [14] Here the operation of simple bubble forming geometries via a pulsating pressure field is considered and Some of the fabricated geometries are shown in figure 5.9. If information is encoded in a bubble sequence, on-demand bubble generators is required to encode this in a channel. The two geometries are based on a T shaped shearing flow device and a cross shaped flow-focusing device. Various applied pressure settings were used to produce different bubble sizes in the channels.

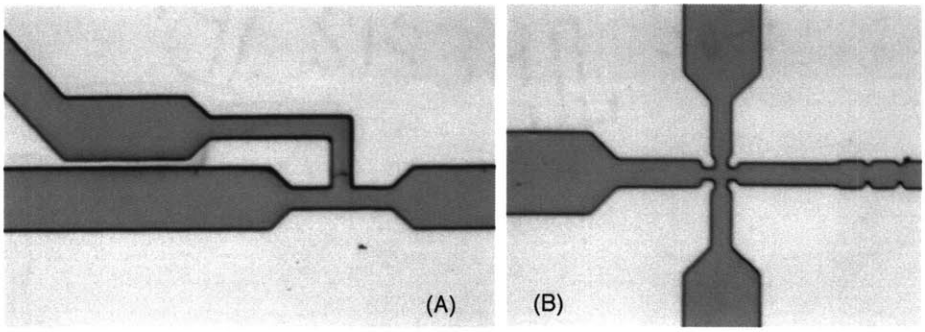

Figure 5-16: On chip bubble generation in microfluidic devices. (A) shows a T shaped shear based bubble generator. The air channel is kept at constant pressure (2psi) while the liquid channel is pulsed from 0 to 1.2psi at a frequency of 1 Hz.

5.10 Bubbble Valves and PMOSFET

In this section bubble gates which regulate pressure inside a micro-channel are described. Applications of bubbles for valving in microfluidic devices was proposed in [26]. No location specific method of generating micro-bubbles was proposed in the above work. This work introduces valving geometries with a UV transparent glass window which allow for 'writing' bubbles at desired location using excimer laser pulses. This provides a way to generate micro-bubbles of tunable sizes (based on number and frequency of laser excitation).

The bubble once trapped remain in the confined geometry. They can be used effectively for valving action in microchannels since they conform to a given geometry thus providing a tight seal around the channel. Simple principle of energy minimization of a bubble is employed to ensure that the bubble comes back to original position once the control pressure is removed. The bubble at the confined geometry can either be induced using laser cavitation or it could be transfered from an external bubble generator and pushed into the device.

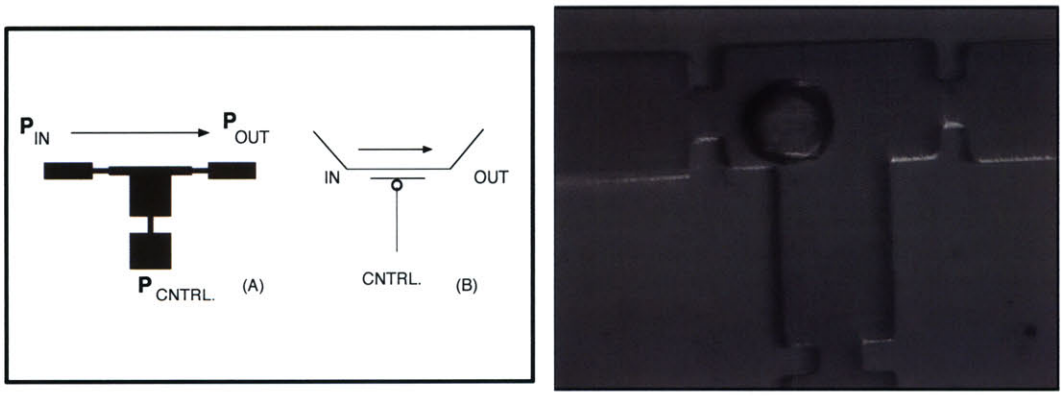

Figure 5-17: PMOSFET gate based on a confined bubble induced in the chamber. The bubble stays in the wider channel if no control pressure is applied. (A)If a control pressure exists, the bubble is forced to cover the narrow region of the channel, thus shutting the flow in the channel completely. (B) Laser induced vapor bubble at the junction. The bubble being smaller than the channel dimension found an energy minima with both control and input flow ON.

The described PMOSFET gate can be used as a valve in microfluidic device. The advantage of such a valve is that it controls liquid flow employing a liquid control

pressure. Thus such valves can be cascaded in series to form complex control functions. Also since the output pressure can be divided into multiple pressure lines, the device has a positive fan-out. The ability of fan-out opens up the possibility of designing complex control networks with interdependent behavior.

Chapter 6

Device Fabrication

6.1 Introduction

In the early era of MEMS design and production, CMOS based chip design and fabrication techniques provided a fast and easy route to producing Micro-mechanical structures. Most of the devices were built in silicon since the process technology for silicon had matured over time. Slowly, as application areas for MEMS devices started growing, new materials and processes for the same were introduced. Currently a large array of materials can be processed for producing micron-size mechanical systems. Some of the most common materials for microfluidic applications include glass, various polymers including Poly(dimethylsiloxane) PDMS, UV cured polymers, PMMA and so on. The above materials expand the functionality of many MEMS devices and also bring production costs considerably down. The processing technologies also vary from chemical etching, injection molding, contact printing, photolithography, laser micromachining and so on.

In this chapter we will briefly overview rapid prototyping techniques for MEMS structures (focusing on microfluidic applications). We will than outline three fabrication processes evaluated in the thesis: micro-mechanical milling, SU8 based photolithography for casting PDMS structures and excimer laser ablation system for micromachining glass and various polymers.

6.2 Rapid prototyping of micro-electro-mechanical systems

Rapid prototyping of functional MEMS structures remains a challenging research area. Due to ill understood nature of dynamics of structures at small length scale the design process for most MEMS devices is highly iterative. Thus for research settings a process which has the least design, production and testing cycle would be most appropriate. For the above reason several techniques like silicone molding of structures, micro-mechanical milling, contact printing and direct write laser ablation have become very popular. [15] [46]

Cause of ill-understood fluid dynamics in microfluidic channels large number of design iterations are common. This is largely due to variations in surface properties, contact angle hysteresis, multi-phase flow, non-newtonian fluid dynamics and multi-physics problem domain involved in many applications. Thus prototyping techniques for microfluidic device fabrication with a fast turn around time are extremely important. Rapid prototyping of microfluidic devices will require

- Effecient CAD tools for microfluidic circuit layout
- Rapid fabrication techniques in microfluidics

An open source printed circuit board design package, Eagle (from *CadSoft*) is used for microfluidic layout and mask design. Thus a library of fluidic components is built which can be reused in different fluidic circuits. For the work reported in this thesis, I explored three distinct process for rapid prototyping of microfluidic devices. First, micro-mechanical milling with high-precision and high-repeatability stages for producing molds for microfluidic devices is discussed. I than move on to discuss the technique of soft-lithography, and the process flow used for the same. Process characterization done on a excimer laser micromachining system to fabricate microfluidic devices in boro-silicate glass and other polymers.

6.3 An Open source layout tools for microfluidics

One of the limitations that a newly born field has to face is the tools available to researchers in the field. This also applies to microfluidic layout. There exist a number of very mature layout tools for microcircuit layout and design including Tanner tools, Cadence and so on. The same is not true for microfluidic layout which is usually done using common CAD tools like AutoCAD, Solidworks and so on. What these all purpose CAD tools lack is the notion of circuit design and routing which is important for a fluidic layout.

Here a flexible open source PCB layout tool, Eagle, was adopted to build library of microfluidic parts on the same. Since microelectronic components have a footprint associated with them, it could be used to define microfluidic geometries. Thus a large number of microfluidic components could be put together in a PCB tool, with useful functions like auto-routing, design definition check for a fixed resolution mask and fabrication process. Since PCB layout tools allow making multi-layers for various layers on the board, it could be easily used for multilayer microfluidic devices. This library consisted of common layouts which are used in many designs. A new microfluidic mask layout can be thus easily created by routing the components from the library. Finally since it is an open source tool, it makes microfluidic layout accessible to everybody conducting research in the area.

6.4 Micro-mechanical milling

Mechanical milling is by far the most important fabrication process used for producing 3 dimensional macro-size parts in the industry, just next to sheet metal forming. Cause of the relative ease and capabilities to produce true 3D structures it holds great promises in the micro domain. There has been recent uprising interest in physics of micro-mechanical milling and its relation to grain boundary of a material. We consider using carbide tool bits shaped on a focused-ion beam as the tool bit for the described machine. [9][11] [32]

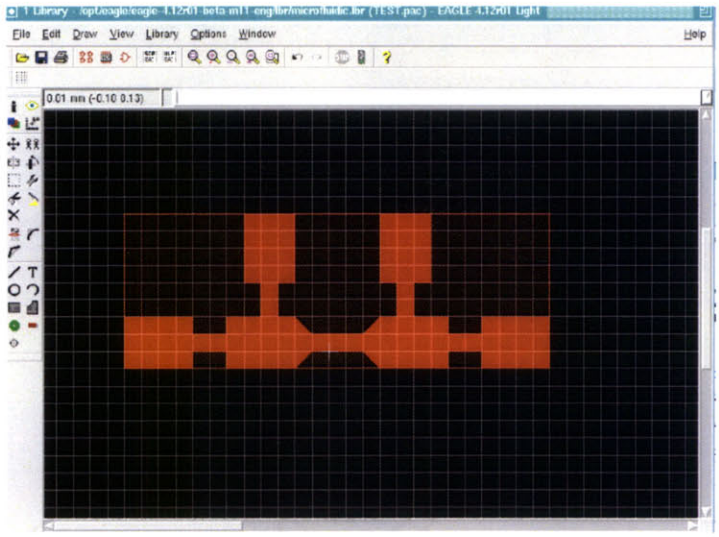

Figure 6-1: A library component displayed in a screenshot in Eagle(CadSoft). Large number of parts can be easily put together in the PCB layout and mask files automatically generated for the same.

We reviewed the available CNC platforms for micro-mechanical milling. An ideal setup would have a high resolution (sub 100nm) and high repeatability (sub micron) with a large travel range (greater than a cm). Based on the functional requirements of the system, we designed and fabricated a micro-mechanical milling platform for the above purpose.

The miniature milling machine was designed and fabricated. Preliminary tests were done to characterize the travel range and resolution for the machine. A high speed spindle needs to be incorporated on the machine to be able to do machining tests. An air-motor based high speed spindle (20K rpm) was designed for the same purpose. In the future we will be doing more characterization tests on the machine, to predict the usefulness of a micro-milling machine for 3D fabrication. A XYZ 3 axis flexure stage was designed for the machine. Flexure stages have an advantage of high resolution of motion, only limited by the resolution of the driving actuator. Moreover, since several mechanical amplifiers can be designed in the stage itself, the range of motion can be tailored to the requirements. A stacked design was chosen with a XY flexure stage [2] mounted on a kinematic coupling linked to a Z stage. Miniature DC

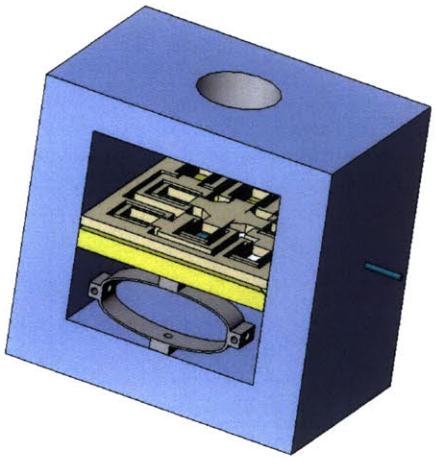

(a)

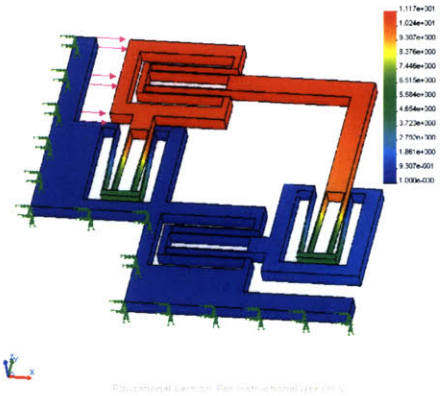

(b)

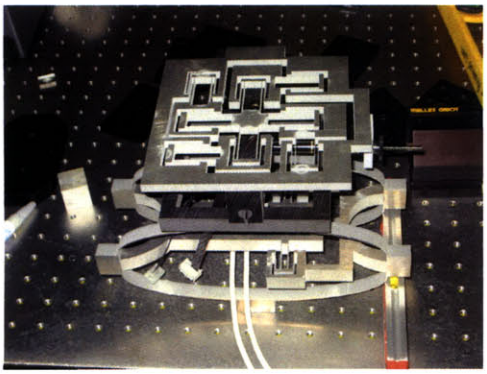

(c)

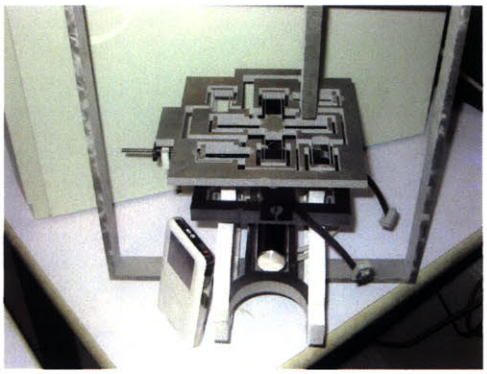

(d)

Figure 6-2: A very high-precision 3 axis flexure-based high-rpm milling machine was designed and built by the author(a) Basic CAD model of the proposed pocket milling machine. The figure shows a XYZ flexure stage, with a kinematic coupling used for stacking. Two actuators are used for XY motion while the third actuator is used to provide Z motion. An air-motor forms a high-speed spindle for the milling machine. (b) Finite element analysis on an asymmetric XY stage. Coupling between the two axis is clearly seen from Y motion of the stage induced due to a pure X actuator motion. Several XY stages were tried based on the criteria of getting a long travel range (c) Precision milling machine based on a 3 axis (XYZ) flexure stage, designed and fabricated. The travel range covers a volume of 1cm by 1cm by 1cm cube. (d) Precision milling machine compared in size with an iPod

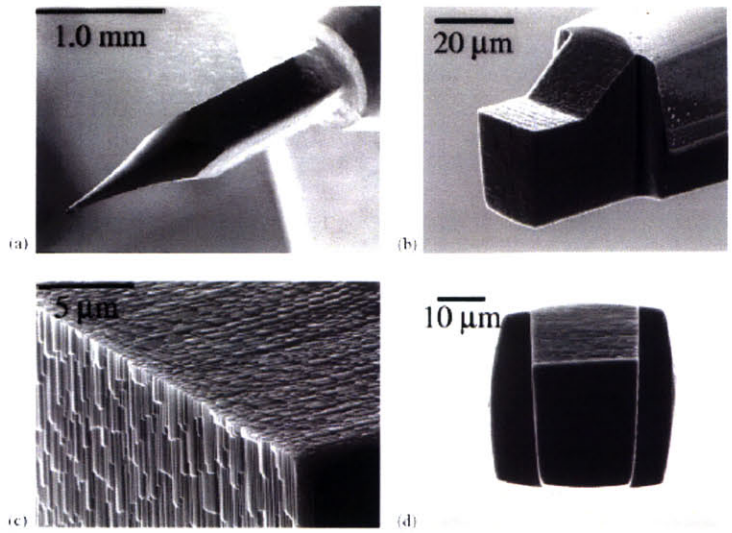

Figure 6-3: SEM micro-graph of miniature milling tools shaped by a focused ion beam for use with a high-precision milling machine (from Picard et al. [32]). Such custom built tools can be used for rapid-prototyping microfluidic structures with variety of channel geometry.

FRADPARC for Pocket Milling Machine

Functional Requirements	Design Parameters	Analysis
1. 6axis / 3axis milling machine	Physics of operation	
2. Range X, Y = 2cm	Subtractive :	Modeling of machining process
Z = 1cm	Rotating tool based machining	eg. Optimization of tool geometry for small tools
3. Tolerance = 100nm	Electrochemical milling with ultrashort voltage pulses	Stress analysis on tools for micromachining
4. Total size = 5cm by 5cm by 5cm	Aditive	
	Two photon absorptive polymerization	
	Mechanics for stage	FEM analysis
	Compliant mechanism based 6 DOF stage	First Order calculations
	Air bearing based XY stage (size consideration ??)	
	Pneumatic motor for compact spindle	
	Configuration	Kinematic Models
	Polar	parallel Vs. serial mechanisms for XYZ stage
	X riding on Y- workpiece , Bridge for Z -tool	
	Workpiece fixed, XYZ tool	

Figure 6-4: FRADPARC sheet describing functional requirements, design parameters, analysis and references for a pocket milling machine

motor was installed in the stage (from Maxon motors Inc.). A tight feedback control loop around the actuator can be used to provide the required resolution for various applications.

The milling tests were down on a polished, high precision aluminum blanks. They act like molds for casting milled structures of the blank. A desktop 3 axis milling machine was used to characterize four-flute milling tools. The smallest tool used was a 5mil flat end mill, while the largest tool was a 30mil end mill. These are commonly used for prototype circuit board fabrication. The turn around time for machining is usually 15-30 minutes based on the amount of substrate to be milled. Smaller feature sizes (smaller than the tool bit) can be machined by milling a channel from two sides, thus creating a negative of the required channel. The machined structure can be easily molded in a variety of polymers to produce the final device.

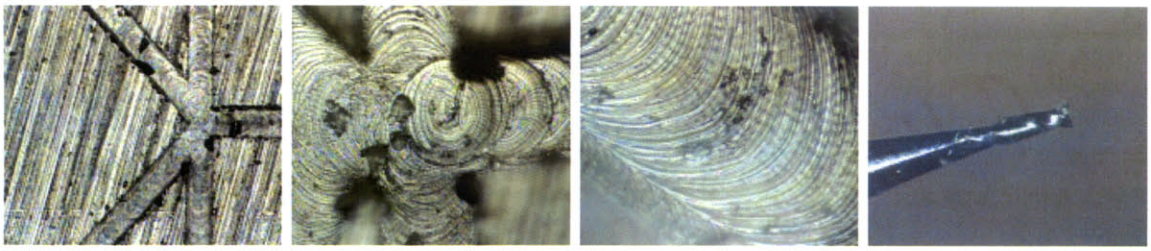

Figure 6-5: Micro-mechanical milling of precision ground aluminum blanks using a flat and round bottom two-flute end mills. Channel dimensions $\sim 500\mu m$ width, $2mm$ in height. A 20 mil flat end mill is shown after the milling operation. Processing time for milling is usually 30 minutes.A 3K table top CNC machine Modela MDX20 was used for the above operation.

6.5 Soft lithography

Soft Lithography has been a very promising technique for microfabrication for the fluidics community. Pioneered by Whitesides group [45], soft lithography involves replica molding of a elastomeric material to fabricate stamps. The polymer used for the microfabrication is Polydimethylsiloxane(PDMS), which has excellent adherent properties to silicon, glass and many traditionally used substrates. Starting from

a transparency mask, microchannels of complex geometries can be fabricated in a matter of hours. Soft embossing techniques and its derivatives [46] have shown that it is possible to fabricated microchannels and geometries reaching nanometer scale using above mentioned technique. Thus the advantages of soft lithography include rapid prototyping, ease of fabrication and biocompatibility.

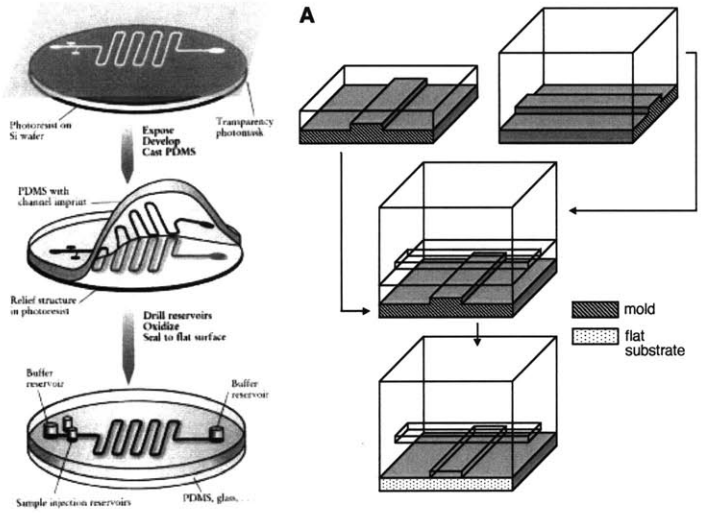

Figure 6-6: Soft Lithography using replica molds PDMS and Multi-layer soft lithography. (a)The principle of replica molding of soft materials in illustrated; from [45]. (b) Multi layer soft lithography extends the above technique by making possible bonding of several layers of patterned surfaces to form a complete device.[41]

We start with a silicon wafer and coat SU8-10 with a spin coater. SU8 is pre-exposure baked to initiate some cross linking prior to exposure. The film is exposed with a negative mask and a UV light source. After a post-exposure bake, the wafer is developed in SU8 developer, leaving the exposed areas on the wafer. After a post-exposure clean in IPA, the wafer is used as a master mold to fabricate PDMS (1:7 ratio polymer vs. curing agent)devices. The mold is coated with silane in vaccum, to avoid PDMS cast sticking to the master mold. The PDMS device is cured in a furnace for an hour at 60 deg C. Once the polymer is completely cross linked, the device is punctured to provide access holes for the channels. Finally the surface of a glass slide and the bonding surface of the polymer are oxygen plasma activated which enhances the bond strength between the two. Finally the device is packed using Intramedic polymer tubing which self seals due to elasticity of PDMS.

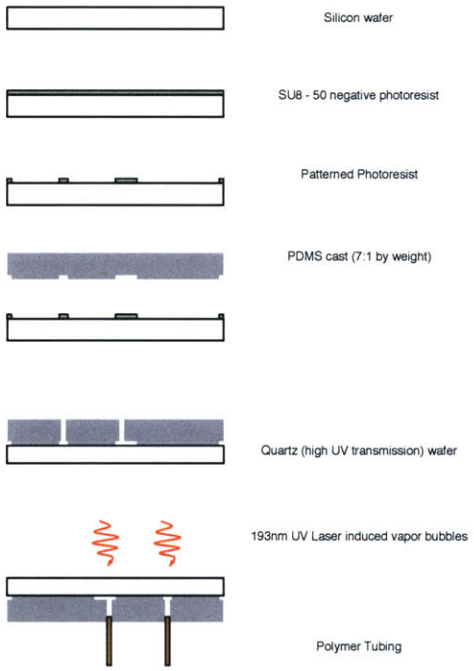

Figure 6-7: Process flow adopted for SU8 based soft lithography. Bubble cavitation is induced by laser pulses.

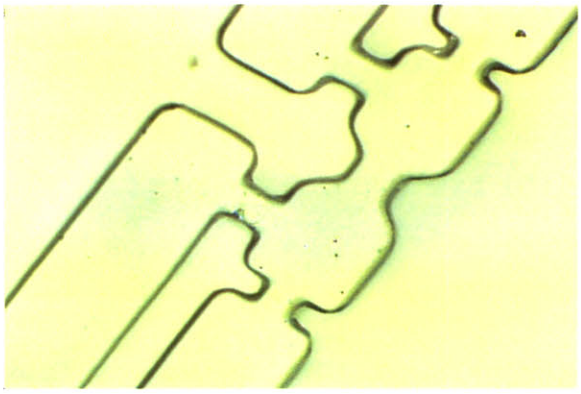

Figure 6-8: PDMS cast from SU8 master after development. Based on exposure conditions and mask resolution, sharp features like corners can get blurred out.

6.6 Direct-write laser micromachining

Laser micromachining is a subtractive direct-write process that can write small feature sizes by focusing a laser beam at a very small area. Direct-write techniques provide increased flexibility, speed for rapid prototyping and material development.

Laser based processing has several advantages for direct write applications. [33]

- Spatial coherence : compatible with small target feature size
- Phase and time coherence : overcoming heat dissipation and high time resolution
- Monochromatic : control over depth resolution
- Site specificity : energy deposited locally

The above advantages can be used by good control over laser intensity and dwell times for the beam. Because of the above advantages, laser micromachining finds immense use in industrial manufacturing processes including laser drilling for high density interconnects, pealing optical fibers for telecommunications, prototyping microfluidic devices, laser trimming calibration sensors, machining catheters and so on.

6.6.1 Physics of Laser ablation

Laser beam interaction with a substrate surface induces series of phenomena which characterize how energy carried by photons is absorbed by the substrate. The above mentioned interaction is highly specific to the laser radiation wavelength, pulse length and energy. Various electronic / vibrational modes are excited after energy from a laser pulse is absorbed by a material. The relaxation path taken by the excited modes determines the kind of effect that will be induced on the surface, ie. heating, melting or vaporization of solid substrate. For high energy excimer lasers, very little localized heating is induced, while the material is vaporized forming a void. The vaporized material often gets ionized and causes a plasma plume. The plasma shields

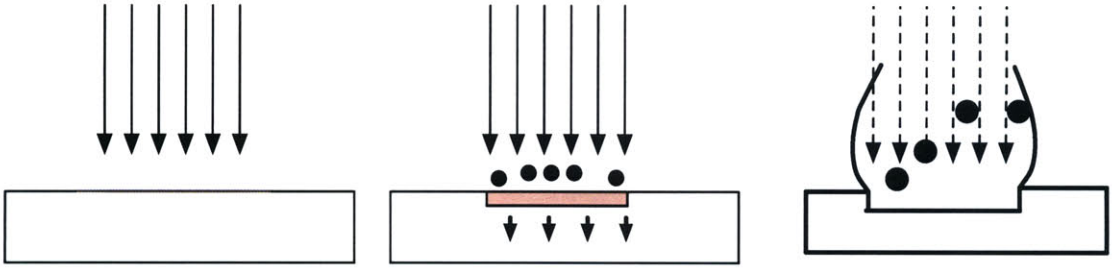

Figure 6-9: Ablation induced by laser pulse. The three stages shown are absorption of laser radiation, melting and vaporization and plasma generation which shields the laser pulse.

the surface from the laser beam. The above mentioned steps describe the process of laser ablation.

A single laser pulse removes a controlled amount of material from a surface. The shape of the feature is defined geometry of focal spot. Ablation depth, δ is a function of laser fluence F (laser pulse energy over spot area (J/cm^2)). For micromachining in the laser ablation regime, the critical factors to be accounted for include Laser fluence (J/cm^2), intensity (W/cm^2), irradiation dose, surface morphology, bulk defect density and thermal conductivity.

$$\delta = \frac{1}{\alpha} \ln(\frac{F}{F_T}) \tag{6.1}$$

where F_T is threshold fluence, below which no ablation is observed. The fluence from excimer lasers usually varies from 0.1J/cm^2 to couple J/cm^2, thus providing an etch rate of 0.01μ/pulse to 1μ/pulse. For a gaussian circular beam, the theoretical minimum radius w_0 at focal point is given by

$$w_0 = \frac{2\lambda f}{\pi d} \tag{6.2}$$

where λ is wavelength of the laser beam, d is limiting aperture before the focusing

lens and f is focal length of the lens. Depth of focus for the beam is given by DOF

$$DOF = \pm\frac{\pi w_0^2}{\lambda} \tag{6.3}$$

6.6.2 System description

The laser used in the system is a pulsed excimer laser. They differ from common continuous wave lasers cause the dwell time of pulsed lasers is very small (in nanoseconds). Briefly the tool comprises of a pulsed laser source, a computer controlled shutter (variable 2 axis aperture), triggering scheme, laser-beam shaping and delivery system and a computer control precision multi-axis stage.

The laser used for micromachining is PM848 from GSI Lumonics. It is a pulsed excimer laser with two switchable wavelengths (193nm and 248nm) based on the gas mixture used in the laser cavity. The laser cavity can be filled with a recipe for KrF (248nm) or ArF (193nm) which swaps the laser wavelength. The system optics including the front and rear end optics for the laser cavity, beam splitter in front of the laser beam, three mirrors for guiding the laser beam, all need to be changed while swapping the wavelength. Demagnification from 5X to 35X can be achieved using doublet focusing lens to direct write features ranging from 1mm to 5 microns. A computer controlled 5 axis stage is used to position and scan the substrate while the laser beam remains stationary. This makes writing complex 2D and 3D structures in various materials possible. The system is equipped with an off axis camera for inspecting the machining process. Typical fluence achieved by the KrF laser is $0.1J/cm^2$ while for ArF it is $0.05J/cm^2$. With a high demagnification, the target fluence can be varied from 0 to $30J/cm^2$. This covers a whole range of materials which can be processed whose fluence threshold is below the maximum fluence possible from the laser. The repetition rate for the laser can be varied from single shots to 200Hz, while a single pulse width is roughly 12 to 20 ns. The maximum energy for a single pulse for KrF laser is approximately 500mJ while for ArF laser it is 150mJ. The system is also equipped with a 2 axis variable aperture for changing the imaging aperture while the substrate is being imaged. This gets rid of double

pulsing effects as seen in figure (6.7.2)

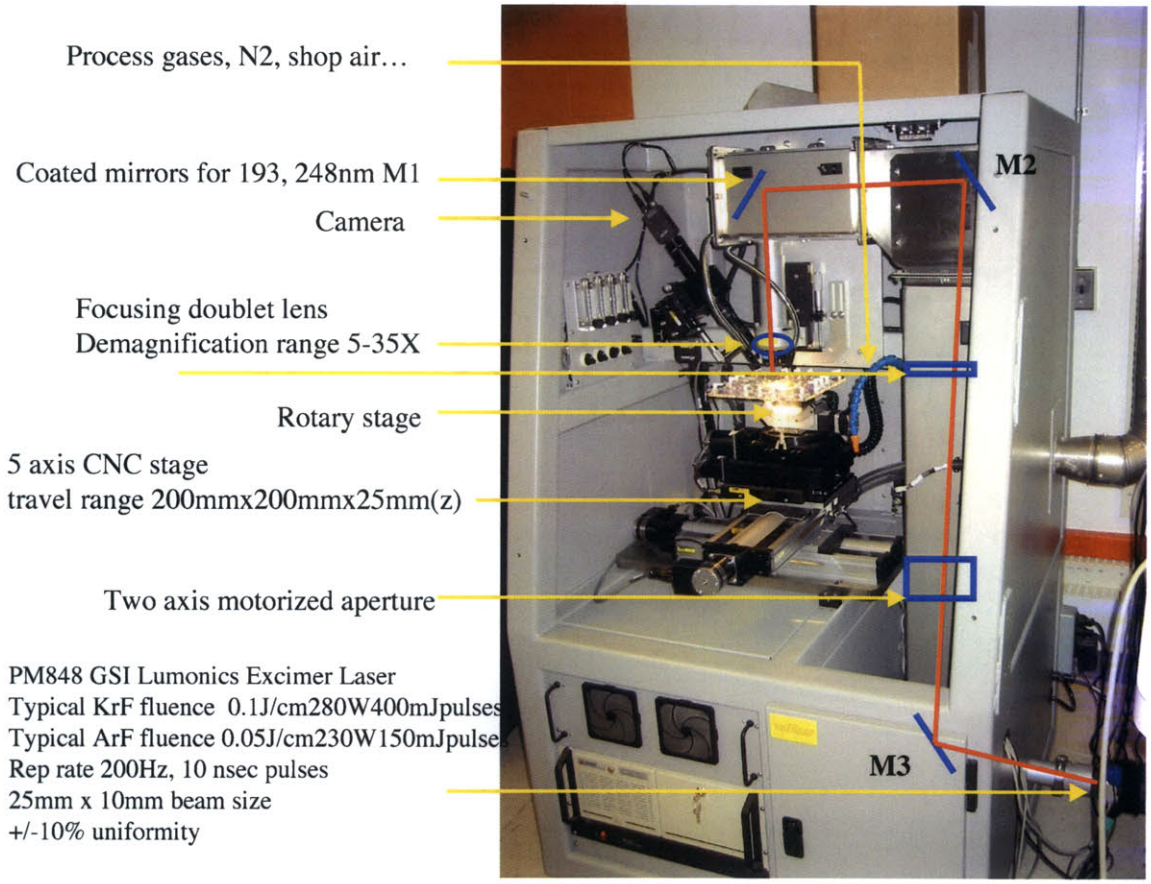

Figure 6-10: Resonetics laser micromachining setup with description of the basic components

Beam propogation

Here we consider simple evaluation of beam delivery based on a gaussian beam profile. Though the system is designed to deliver a flat top homogenized laser beam profile(6.6.2), for simplicity we will consider a gaussian laser beam propagating in a diffraction limited optics for the following analysis .[33] Thus for propagation axis z, $\omega(z)$ is the radius function for the beam while the wavefront curvature can be given by $R(z)$.

$$\omega^2(z) = \omega_0^2[1 + (\frac{2z}{b})^2] \tag{6.4}$$

$$R(z) = z[1 + (b/2z)^2] \tag{6.5}$$

$$b = 2\pi\omega_0^2/\lambda \tag{6.6}$$

where, λ is the wavelength, ω_0 is beam radius at waist, b is confocal parameter.

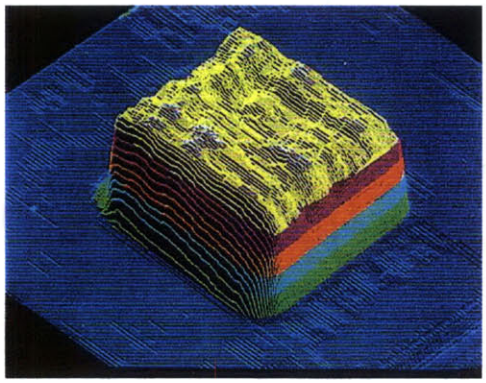

Figure 6-11: Top hat shaped laser beam intensity profile coming from a excimer laser. The beam is shaped such that the intensity is uniform over the surface of exposure.

For a focusing system with focal length f, and an aperture D (where f number is defined as f/D) we have minimum beam diameter given by

$$d_0 \approx 2f\lambda/D \tag{6.7}$$

$$DOF \approx 2\pi(f/D)^2\lambda \tag{6.8}$$

Thus for a 248nm wavelength laser beam, and focusing lens with f number 2, minimum spot diameter is $\sim 1\mu m$, while the DOF is $\sim 6\mu$m. As above, though beam diameter is proportional to the f number, the DOF is quadratic in f number. Thus very small f number may be limiting in machining applications, since the DOF reduces to a small number. This makes the task of keeping a substrate in focus extremely difficult.

Also the resolution of the system is defined as R where

$$R = \frac{C\lambda}{N.A.} \tag{6.9}$$

$$Z = \frac{\lambda}{N.A.^2} \tag{6.10}$$

where $N.A.$ is numerical aperture of the imaging system, which specifies light gathering power of the system.

Table 6.1: Etch rate for common materials

Material	ablation depth (μ)
Polymers	0.3 to 0.7
Ceramics and glasses	0.1 to 0.2
Metals	0.1 to 0.2

6.6.3 Etch rates

The above table (6.1)shows typical numbers for ablation rates for strongly absorbing materials using a KrF 248nm excimer UV laser.

6.7 Excimer laser ablation results

Various devices were fabricated using the excimer laser ablation. A large set of materials can be used to fabricate microfluidic devices. We started with borosilicate glass, cause of its good machinability properties, excellent optical clarity, and good mechanical strength. Process tuning for machining borosilicate is described in the following sections. Channels as small as 30 /*mu*m were fabricated by scanning a square aperture over a substrate. Access holes were machined by the same process. The wafer thickness chosen was 170 /*mu*m. Post cleaning was often necessary due to some glass debris which are left in the channels. The glass wafer was cleaned in a ultrasonic bath for 30 minutes. Various wafer bonding techniques were tried to seal the micro-channel. PDMS blank was bonded to the glass surface using oxygen plasma activation. Glass to glass anodic bonding has been reported in literature. In the near future we will try out glass to glass anodic bonding for fabricating multilayer chips. Characterization of most of the fabricated channels was done using a materials testing confocal microscope in scanning mode. Thus 3D structure of the machined part can be easily obtained from the substrate, which provides a good characterization tool for laser micromachining.

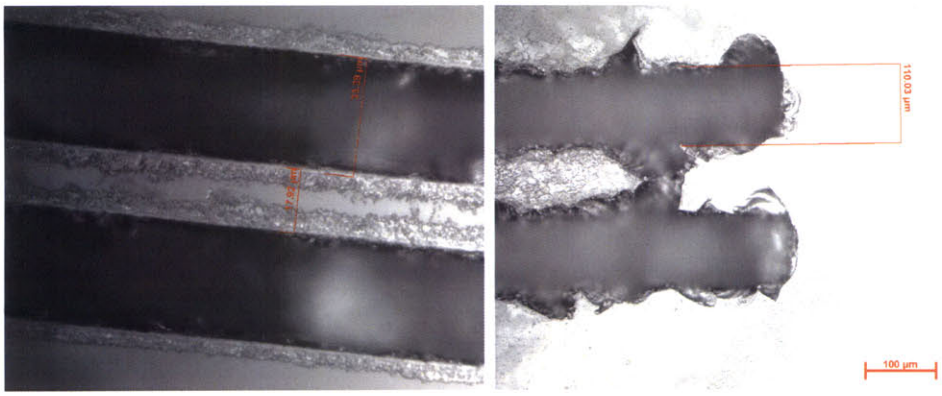

Figure 6-12: Difference between laser ablation with change in wavelength (a)193nm resolution tests in borosilicate. Channel size 30 microns (demagnification factor 29), 30kV @ 50 hertz. The deposits at the channel edges can be cleaned by ultrasonication. Some debris can be seen in the channels. (b)Borosilicate ablation at 248nm. The two channels have cracked side walls. (28kV@100Hz, 110 micron channels)

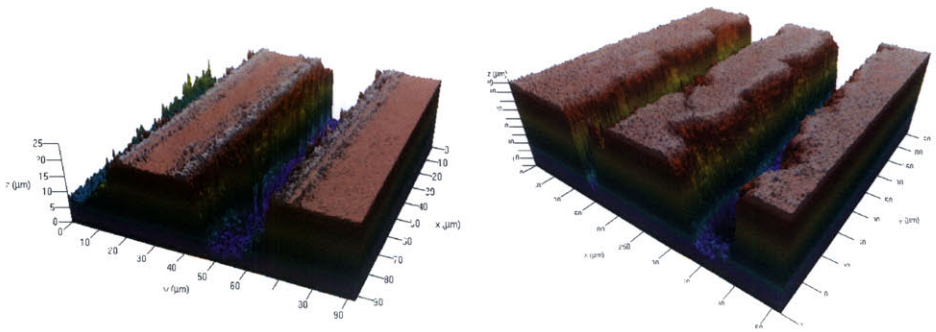

Figure 6-13: 3D surface images and plots using a Confocal microscope (a)193 nm ablation of borosilicate, 20 micron deep channel. No cracks visible at the edges. Pre cleaned smaple. 30kV @ 50Hz. X bar = 90 micron, Y bar= 90micron, Z bar = 20 micron (b)248nm resolution tests in borosilicate glass. 90 micron channels were ablated in 170 micron thick glass cover slip. The structure was imaged using a confocal microscope. Cracks at the channel edge are clearly visible indicating unsuitability of wavelength choosen (248nm) for ablating borosilicate glass. X bar = 500 microns, Y bar= 500 microns, Z bar= 100microns.

6.7.1 Frequency dependence of laser ablation

Excimer laser ablation is a photolytic (photochemical) phenomena. Thus the changes induced by a laser pulse on a material can be frequency dependent which provides a greater control over the process. An example of frequency dependence is clearly seen in laser ablation of boro-silicate glass using a 193nm pulsed ArF excimer laser vs. a 248nm KrF pulsed excimer laser. Cracks induced on the edges of a micro-channel in borosilicate glass with 248nm pulses can be clearly seen in figure (**??**, **??**). The figures clearly indicate minimal damage occurs to the channel edges for 193nm processing setup.

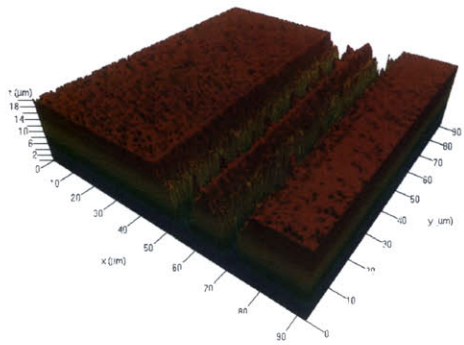

Figure 6-14: 248nm resolution tests on polycarbonate. The two scans were offset by a 10 micron movement in Y direction. 20 microns deep channels 10 micron apart. X bar = 90 microns, Y bar = 90microns, Z bar= 20 microns

6.7.2 Laser machining complex 2D and 3D geometries

Various strategies can be employed to produce complex 2D and 3D geometries in various substrates. The two modes the laser can be used are scanning direct write mode and mask based single exposure mode. For scanning mode, the CNC stage holding the work piece is continuously moved while the beam delivery is on. This mode can be used to direct write a complex pattern without using a chemically etched mask as a starting point. Thus fairly complex structures can be easily written by CAM programs which control the stage.

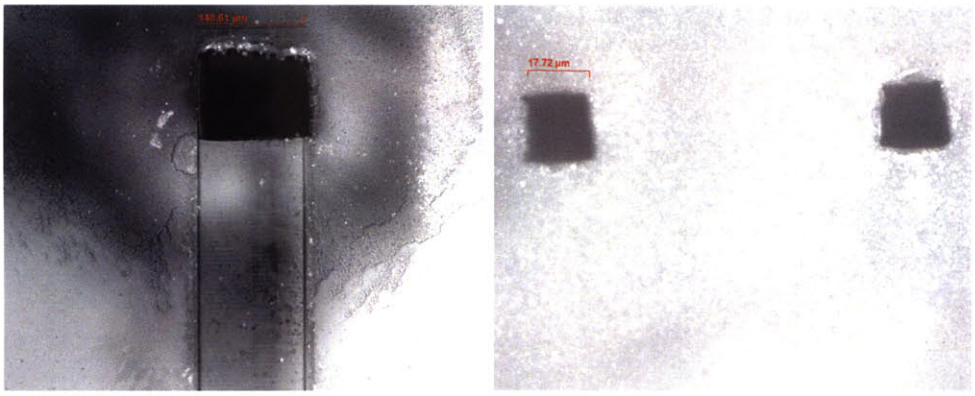

Figure 6-15: (a)140 micron wide, 10 microns deep microchannel with an entry port machine by a 193nm excimer in borosilicate glass, 170 micron thick (30kV @50Hz, demag= 29, scanning mode, 10 shots per image for channel). Post cleaning done by ultrasonication. (b) Through holes in 170 micron borosilicate glass, 33kv@5oHz. Total shots 2500. 20 micron exit holes shown in the figure above, pre cleaning. No debris on the exit holes.

A disadvantage of scanning mode direct write ablation is irregular laser intensity on the substrate. Since the ablation depth is a very strong correlation of the laser intensity (Fluence) at the substrate, average intensity for a deried flat feature must be kept constant. If Multiple passes are made through a common region, some regions can be exposed more than once, thus resulting in irregular bottom surfaces. This is illustrated in a simple example of machining a "L" shaped channel. (6.7.2) To produce a flat bottom surface, the laser intensity of the beam should be varied such that final exposure is a constant over the entire region. This is accomplished by regulating opening and closing of a 2 axis variable aperture system before the focal optics.

The above limitation can be used to our advantage for producing 3D features using laser ablation in scanning mode. For example, control over channel geometry for a microfluidic channel is shown in fig (6.7.2). A circular bottom micro-channel was produced by using the laser in scanning mode with a circular aperture being used as a mask. Since the laser intensity is highest at the center of the channel and falls of at the edges, a semi-circular micro-channel is produced in a single scan cycle. Other methods of producing semi-circular channels like photo-resist reflow are fairly complicated and require a tight process control. The same technique can be used to

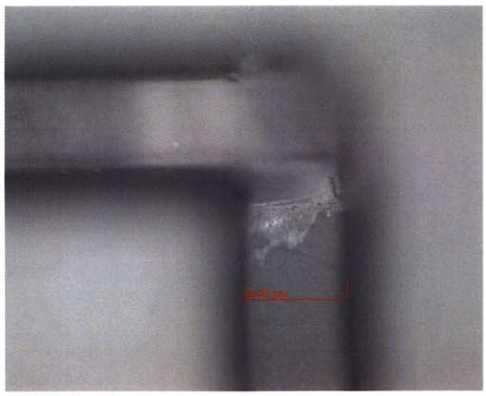

Figure 6-16: 193nm Borosilicate, L shape channel. Focused at the bottom. Flat bottom with deeper groove at the joint. This is due to higher effective laser intensity due to a sharp turn which causes a longer dwell time at the joint.

produce a variety of channel geometries including square, "V" shaped (6.7.2) and so on.

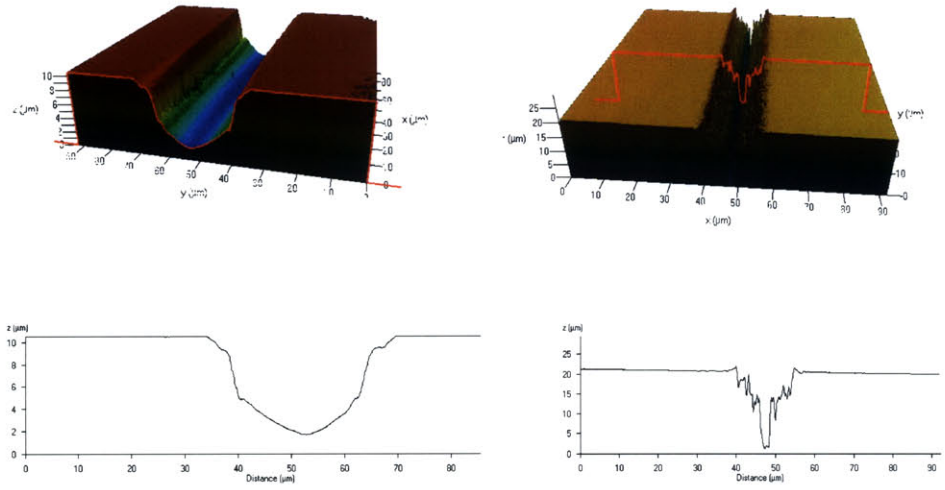

Figure 6-17: (a)Curved channel using a circular mask scanning in X direction. 10 micron deep channel in Kapton@248nm, 5 pulses per image,28kV@50Hz. (b) V shaped channel in borosilicate. A square mask was scanned with an offset to produce the V shaped groove. Imaged on a confocal microscope.

The second mode the laser can be operated in single exposure mask based ablation. Thus a precise macro size mask for the required geometry is produced in stainless steel shim stock using either chemical etching or machining. Once a mask defines the required geometry, it is exposed with a uniform laser beam which produces the structure in a single shot. The resultant surface at the bottom is extremely smooth

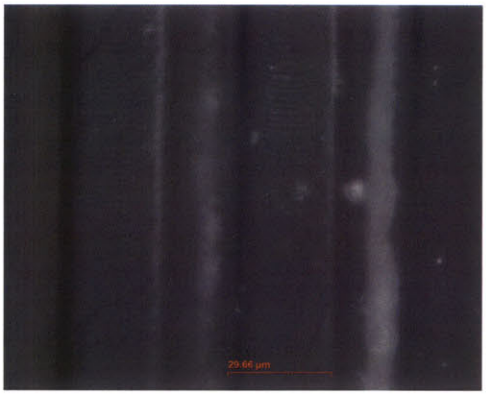

Figure 6-18: Curved channel at the bottom created using a circular exposure mask. 193nm borosilicate glass.

as compared to direct write scanning mode ablation. The masks can be produced by water jet machining or CNC machining a shim stock. Both the processes have a fast turn around and the mask can be produced in house fairly quickly. Using a UV transparent glass, we can also produce free-standing structures which were not possible using a conventional single piece stainless steel mask. For producing free standing structures, a stainless steel mask is sandwiched between UV transparent glass. Fig (6.7.2) shows a complex pattern etched in Kapton using single exposure of a complex mask. The figure also depicts the focusing sequence used to determine the focal point of a setup. An accurate determination of focal point of the laser beam is crucial for correctly and accurately imaging the mask.

6.7.3 Remelt

Materials vaporized by laser induced ablation process is ejected from the void upwards. Solidification of the melt at the edges of ablated feature appears as residue or burr of the ablation process. For machining borosilicate, fig (6.7.3) shows the recast material on the sides of machined channel. Recast material hinders good wafer bonding of machined substrate to another flat substrate. Reduction of volume of melt, strong optical absorption, high fluence and short pulse duration will reduce recast formation.

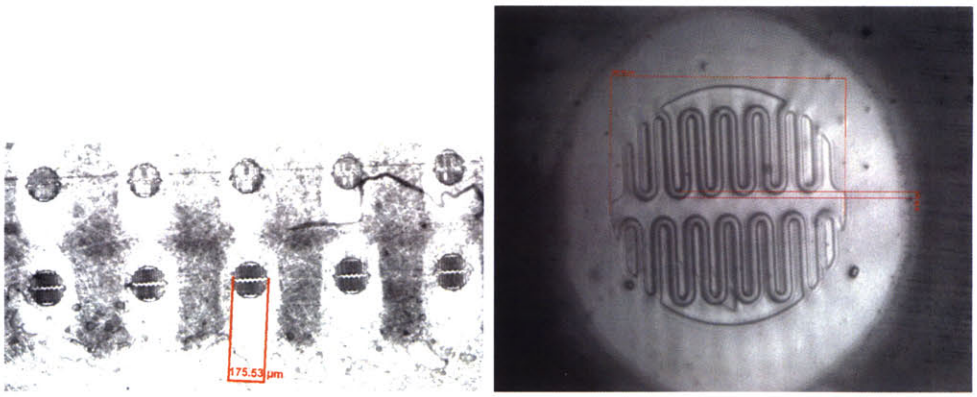

Figure 6-19: (a)Focusing sequence using a high resolution mask with a Z step of 50 microns. Substrate is Kapton, which is stuck the material you want to ablate. 28kV@50Hz, 5 shots epr pattern, 248nm. (b) Focusing task on Kapton, 248nm. Uniform ablation, 5 shots 28kV@50Hz. 350 micron diameter structure, with 10 micron being the thinnest line.

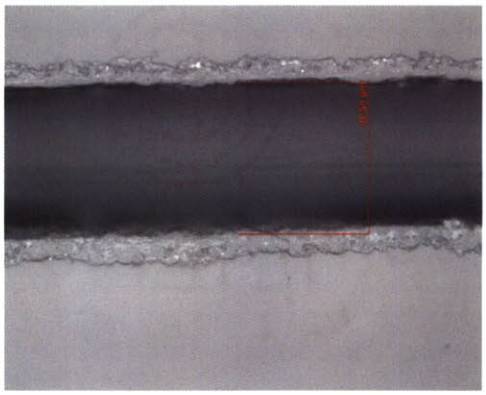

Figure 6-20: Remelting in glass on the edges. 40 micron channel in borosilicate ablated with 193nm, 30kV@50Hz. Post clean.

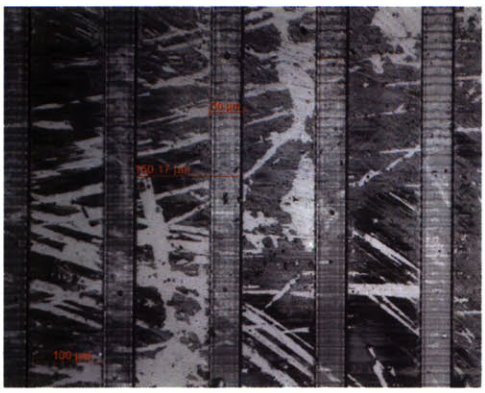

Figure 6-21: Five 50 micron wide channels, 20 microns deep ablated in borosilicate using 193nm excimer 30kV@50Hz. Post ultrasonication in acetone. Entry/exit holes for all channels machined simultaneously (not shown in figure). Scanning marks visible at the bottom. surface rougness O(1 micron).

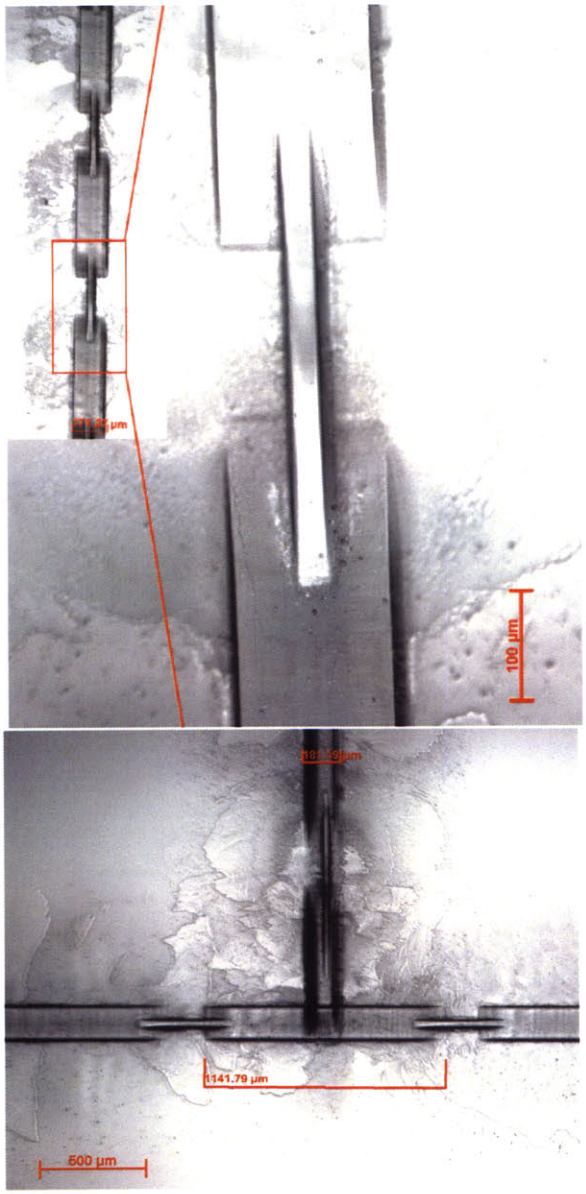

Figure 6-22: (a)Series of constrictions in a channel, machined at 193nm, 30kV@50Hz. Borosilicate glass, post cleaning. End of scanning shows a ramp (in dark regions) due to non uniform laser intensity when a scan starts and ends. This can be corrected by using a programmed shutter in the laser. (b) P fluid FET (open when control gate low, closed when control at high pressure) structure ablated in glass, 193nm. Post sonication.

Chapter 7

Results and future work

In this section results from proposed devices and future work to come, is covered. The fabricated devices were tested in a lab setting via constant pressure, constant flow and pulsating driving flow settings. The chapter first covers results from laser induced cavitation in microfluidic channels. The test setup is described and finally results from individual devices and pressure sensors is covered.

7.1 Laser induced cavitation in microfluidic channels

The mechanism of cavitation induced by a laser energy source is employed to programatically produce bubbles at specific locations in the device. Here the mechanism of bubble formation in microchannels induced by laser excitation is described. See fig (6.5) Two plausible methods for inducing bubbles in microchannels are discussed. Bubbles can be induced with interaction of laser pulses to the ground substrate. The process of ablation under water do not allow the vaporized substrate to escape, which induces bubbles at specified locations. With higher ablation energy surface properties of the substrate can be modified which in turn ties the bubble to a specific location.

Another mechanism to induce bubbles is using a secondary phenomena. Since excimer laser ablation is a non-thermal process, and the chemical bonds are broken

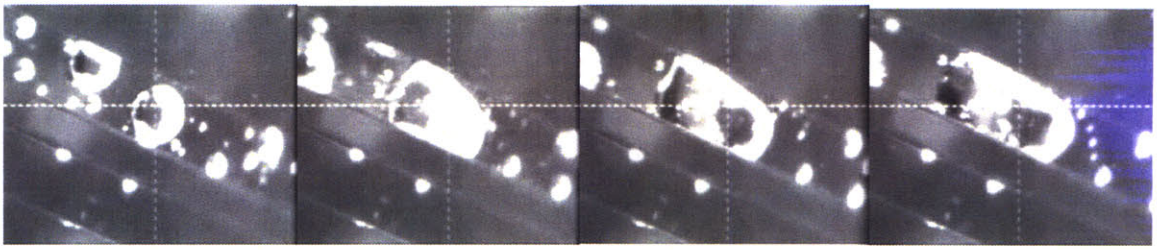

Figure 7-1: Bubble growth (inflation) due to laser induced vaporization. Size of the bubble can thus be tuned to match the geometry by consecutive laser shots.

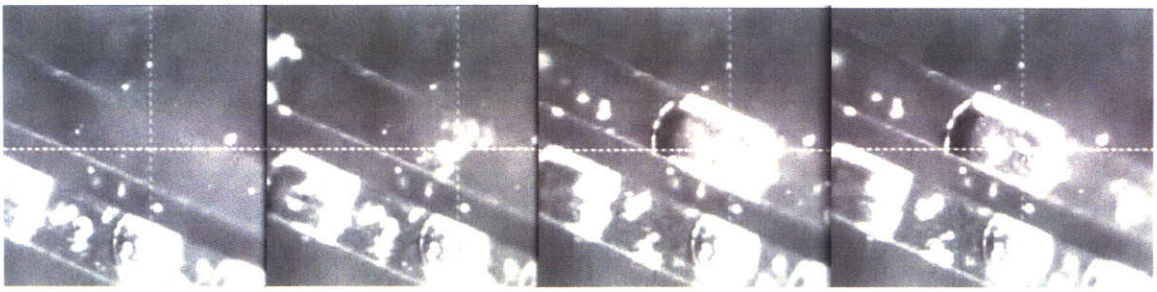

Figure 7-2: Single bubble induced by a series of laser shots. The sequence of micrographs indicate various phases associated with bubble formation, including vaporization, growth and relaxation. 248nm KrF excimer laser induced bubble in water with 1M NaCl solution. 28kV 100Hz 3 pulses in a 100 micron PDMS channels with UV transparent quartz glass sealing.

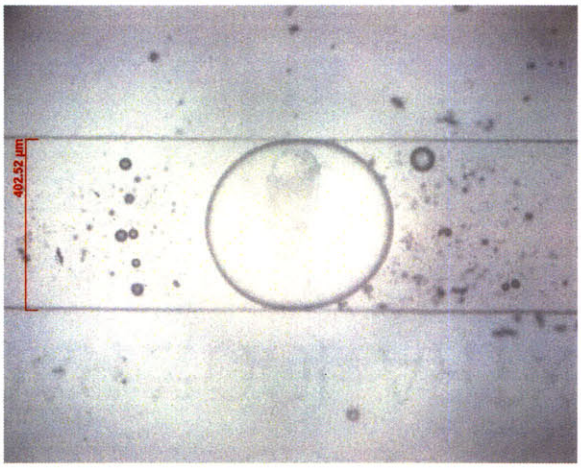

Figure 7-3: Bubbles induced by a 193nm three pulses at 29kV. A large bubble 450micron in size completly covers the PDMS channel.

Figure 7-4: Non circular bubble shape indicating a surface phenomena as a reason for bubbles being tied to the surface. Stability of the bubble indicates surface modification induced by laser pulses.

not by generation of heat, but by directly inducing changes due to high energy content in the beam (targeted photons). Thus Chlorine ions in water are used as a secondary mechanism for generating heat. Free chlorine ions are excited and they emit energy when coming back to ground state. This induces vapor bubbles in aqueous solution. We use a strong iconic concentration of NaCl solution as our liquid medium. The minimum threshold energy fluence needed to cause cavitation in a liquid is known to be directly proportional to penetration depth δ (given by $\delta = 1/\epsilon x C$, where ϵ is molar absorption coffecient of NaCl and C is molar concentration of NaCl).

Thus bubbles could be induced at specific locations in various geometries. The size of the bubble was correlated to the energy fluence from the laser. Bubble stability and collapse was observed as a function of time. Dynamics of bubble formation and collapse in liquid medium induced by laser sources has been studied by Palanker et al.. [40]

7.2 Test setup

Several test setups were fabricated to characterize flow and pressure data from fabricated microfluidic gates. Various driving strategies for the fluidic devices were tested. A simple hydrodynamic constant pressure was used to create a low head pressure for

driving the fluid. Another setup consisted of a gas back pressure on a closed liquid vessel, providing pressures as high as 20 psi. A constant flow rate was used with a syringe pump driving the channels. Finally a time based pressure pulsing mechanism was designed and fabricated to provide a pulsing pressure clock to the devices. a pulsing driving strategy provides precise time control for transport in microfluidic channel, which is otherwise only possible in a digital microfluidic device. A complex fabrication and a non scalable control process is involved in controlling conventional digital microfluidic devices.

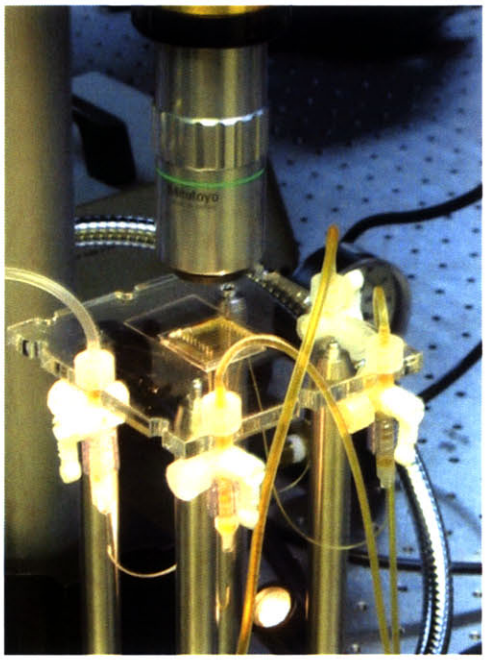

Figure 7-5: Test setup used to characterize fabricated microfluidic devices. Various driving strategies including constant hydrodynamic pressure, constant flow rate and pulsating pressure was used. A medium frame rate video camera is used to image working devices.

A test rig was constructed to switch the devices from the flow setup to the laser and back again. Thus we were able to preserve the pressure settings inside a channel without exposing it to the atmosphere, and in term avoiding drying of fluids inside the micro-channel.

Figure 7-6: Test setup for simultaneously testing a large number of devices. The current image shows 22 access ports which can be opened and closed to access all the input ports to the chip. Two devices could be simultaneously mounted on the rig.

7.3 Bistability

Two kind of bistability was observed in the fabricated devices. One was from memory devices with two chambers connected by a narrow region. Once applied pressure field is greater than the clogging pressure the narrow constriction, the bubble is pulled towards the other channel. Once the center of mass cross the center of narrow region, the bubble is completely pulled to second chamber.

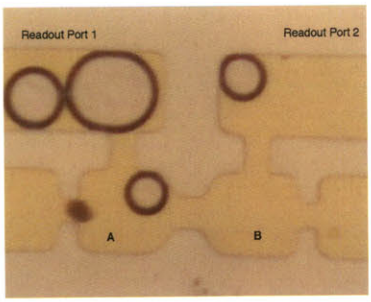

Figure 7-7: Bubble memory constructed with two chambers joined by a narrow channel. The bubble can be switched from one to another by a applied pressure field gradient.

Another kind of bistability in flow was observed in the two phase cross flow device. Here channel B was completly shut as is seen from a static bubble in channel B. Channel A experiences a constant pressure gas and liquid flow (both set at 1.5psi) meeting at a T junction. The switch between flow regimes occurs whenever the air flow thread breaks down, due to shearing water flow.

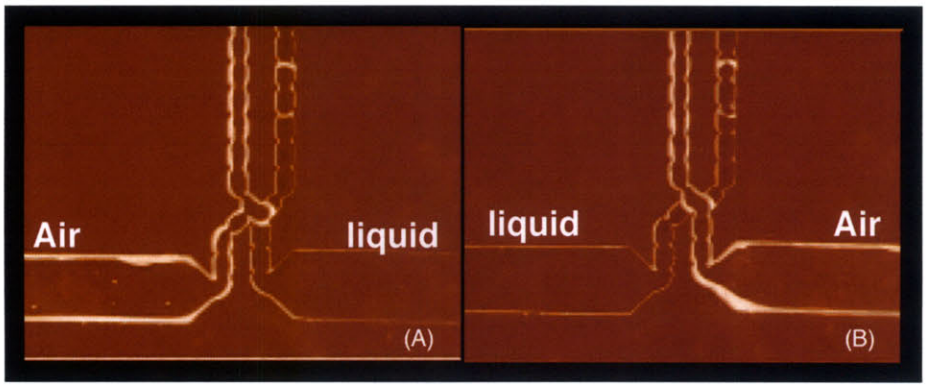

Figure 7-8: Bistability existsing in two phase flow device. Channel A has both air and water flow turned on with a constant pressure. Channel B is completely shut. Transitions from one regime to another happen if the air threads breaks down due to capillarity and shear flow. The colors in the grey scale image have been inverted to highlight the difference between air and water.

7.4 Nonlinearity

To show existence of nonlinearity, multiple AND / OR logic gates have been fabricated. The basic principle behind the logic gates is the notion that a bubble takes a 'path of least resistance'. Thus various channel geometries are constructed so as to induce bubble bubble interaction at the channel junction. In current work, the cross flow AND/OR device was tested. The bubble sizes obtained from the on chip "T" generator were much larger than the ideal size the device was designed for. Thus single bubbles sometimes occupied more than one chamber volume.

Thus if any of A or B channel has a bubble flowing, it prefers to flow thorough A+B. Once two bubbles come simultaneously at the junction geometry, one of them is forced to take the path towards A.B . This is because for both bubbles to travel

to channel A+B would require substantial deformation in bubble geometry, which is unfavorable.

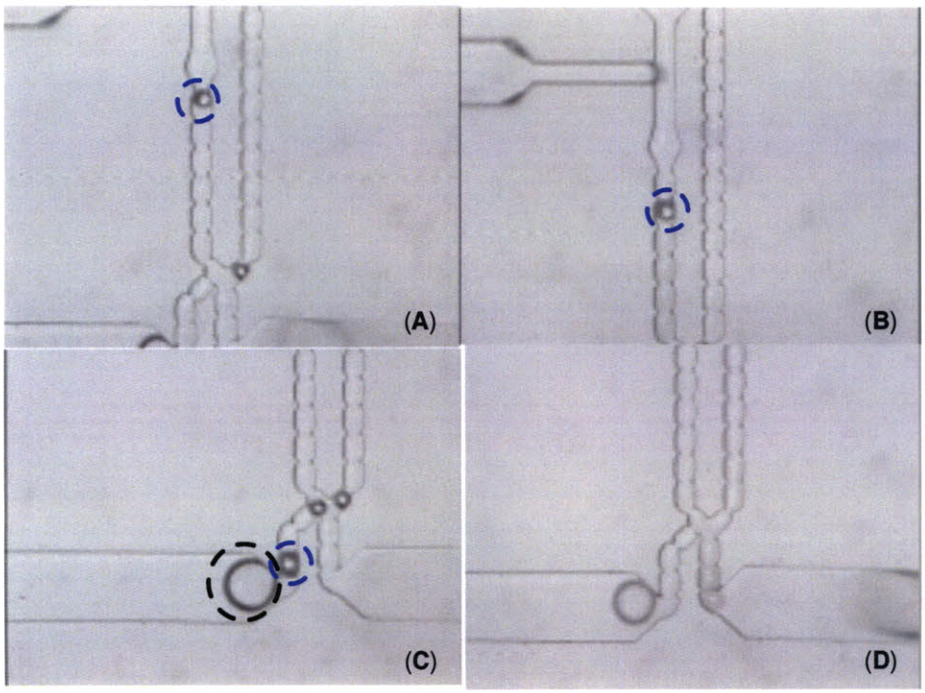

Figure 7-9: An AND / OR gate was tested in a cross flow geometry. Bubbles coming from both channel A and B prefer to flow through channel marked A+B. This is because the constriction at the junction is much wider for the above channel as compared to A.B . Bubble marked with black circle happens to be an air bubble trapped due to sudden expansion of the channel. Bubble marked with blue circle is tracked in different frames.

7.5 On-demand bubble generation

Several fixed frequency bubble and droplet generators based on shear flow have been reported in literature [23] [12] [21] [14]. In this work, I consider a novel method to generate on-demand micro-bubbles in microfluidic channels by a pulsed driving pressure. On-demand droplets generated in microfluidic devices would provide a precise temporal control of reaction timings for droplet based micro-reactions. The liquid driving pressure is pulsed using a solenoid which induces the start of a bubble formation. Thus single bubbles can be formed on demand in microchannels. This

is used as a way to encode information in a series of bubbles generated. Figure 7.5 shows a single bubble dispensed using a square pressure pulse used to drive the air flow, of roughly 2psi. The air side channel is kept at a constant pressure of $\sim 3psi$.

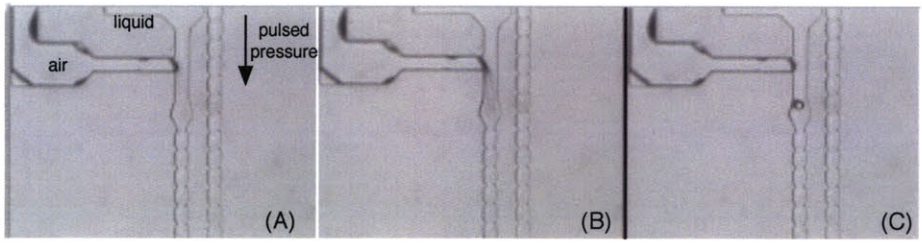

Figure 7-10: On-demand micro-bubble generation in microfluidic devices. A square shaped electric pulse is applied to the solenoid in the liquid channel which generates a pressure pulse. This sudden temporary drop of pressure induces a growth of air interface, which is kept at a constant pressure. Thus at the end of the pressure pulse single bubbles can be generated on-demand.

7.6 Bubble based pressure sensor

As described in section 5.7, a noticeable compression occurs in bubble volume for a change in external pressure. This principle is used to measure pressure of a microfluidic channel at different regions. High aspect ratio channels are used for the sensor such that induced bubbles are completely inside the liquid (thus avoiding any effects due to solid surface). With an ability to nucleate bubbles at specific pressure ports, measurements of bubble diameter give a good correlation to pressure inside the channel. Simple optical techniques can be used for on-chip pressure measurements. From the port geometry, air is inherently trapped inside the pressure ports. Since PDMS is porous to many gases, the gas very slowly diffuses out of the channels (in matter of 20-30 minutes). Currently measurements using an air-water meniscus inside the pressure ports are presented. Since PDMS has a pressure dependent diffusion rate for gases, the meniscus height itself would not give a very accurate pressure reading at a port. Though distribution of meniscus heights is a very good measurement of pressure distribution, since the diffusion rate in all pressure ports is similar.

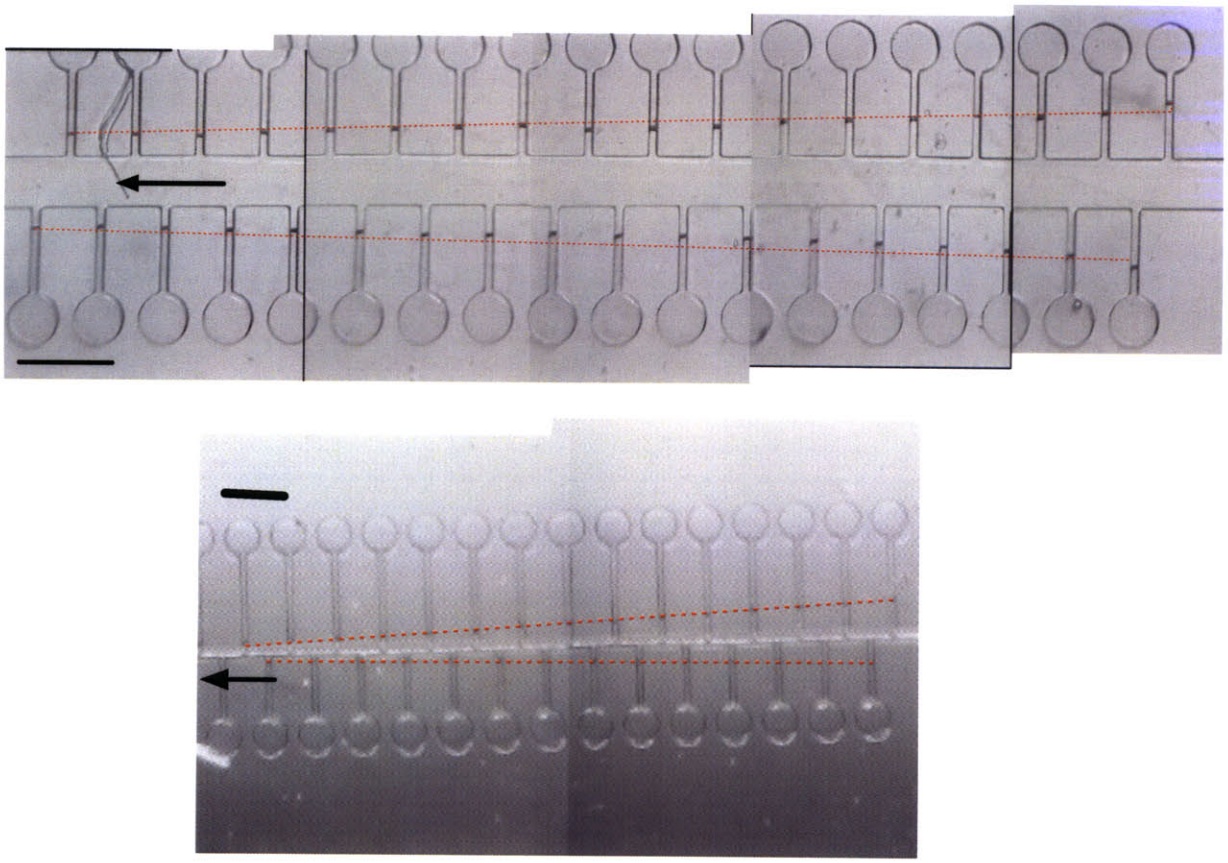

Figure 7-11: Pressure distribution inside a straight micro-channel. Analytically resistance R of rectangular micro-channel is given by $R \sim \frac{12\eta L}{h^3 w(1-0.63h/w)}$ (A) Linear dependence of pressure with channel length inside a micro-channel with a flow rate of $Q = 17.6\mu l/sec$ and a total head pressure of $101.5gm/cm^2$. Channel dimensions are $2mm$ in length, $100\mu m$ in width and $75\mu m$ in height. (B) Pressure distribution in a thinner micro-channel with width $30\mu m$. Scale bar represents $100\mu m$.

Tries to nucleate bubbles inside pressure ports failed due to use of a longer wavelength at very low demagnification ratio. A low demagnification accounts for a lower laser fluence on microchannels. Future work will include work on nucleating bubbles inside pressure ports and measurements from those nucleated bubbles.

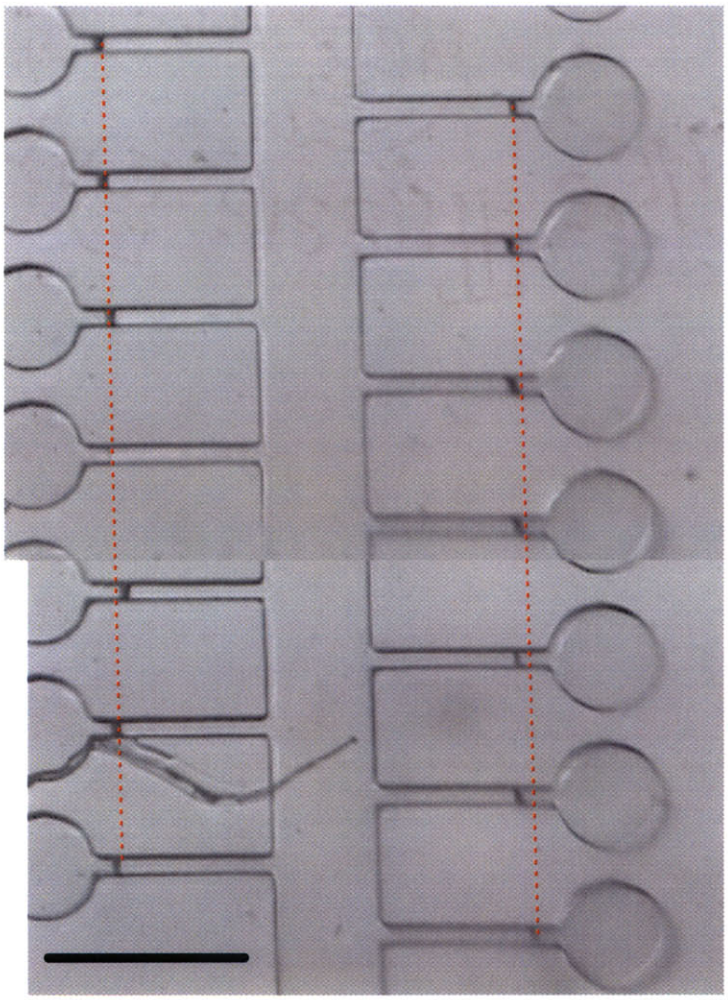

Figure 7-12: Pressure distribution inside a straight micro-channel with flow shut off. Since the pressure distribution should be the same across the channel length, the meniscus bars align vertically.

7.7 Future work

Extensive testing and characterization of the described devices will be performed in the near future. We have currently explored a air-water two phase system. In the

near future a characterization of a water-oil based system will also be performed to see dependence on viscosity (though viscous forces are small compared to surface tension forces in devices described). An optical scheme for the readout of pressure sensors based on laser diodes will also be explored. Since changing the dimension of the bubble also changes its ability to focus a light beam at a point, a simple readout strategy which is completely non-invasive will be designed. Thus a large number of pressure ports could be observed at the same time. Several microfabrication schemes were also explored. Future work will move towards direct writing of microfluidic structures to rapidly prototype and test ideas.

A scheme of pressure sensing using micro-bubbles is proposed in this work. To the best knowledge of the author, it is a first purely mechanical scheme to measure fluid pressure inside microchannels. Further work will be performed on characterizing those devices and measure its temporal sensitivity.

Implementation of described control strategy to specific microfluidic problems will be explored. In near future, characterization and scaling properties of the proposed control strategy will be evaluated using examples from micro total analysis systems.

7.8 Conclusion

Bubbles in microfluidic channels have always been considered an annoyance to a microfluidic engineer. Current work has opened up a number of applications where air bubbles can be employed and used its properties to advantage. With the advent of droplet based microfluidic systems, it is believed that bubble / droplet based control strategy will be very appropriate. All the devices described have no moving parts. A new valving strategy using air bubbles was also proposed in this work. Since the control devices are based on a single layer (no separate control and liquid layer), the devices have a fan out of greater than one. This can be used to design cascaded control structures which are scalable as the number of parts in microfluidic applications grow.

Several implementations of simple logic gates, memory elements and shift registers were fabricated and tested. All the necessary requirement of a scalable computing

architecture were satisfied. Thus all fluidic information processing could be performed using the devices described in this work. Several applications require very high immunity to electromagnetic radiations. Since the system is designed to work only with fluid flows, effects like electromagnetic radiation, reasonable high operating temperature does not hamper the functioning of these devices.

Another contribution of this work is design, fabrication and testing of a microbubble based pressure sensor. Getting pressure readings in microfluidic channels has always been very challenging. The current work proposes a simple scheme to measure pressure inside micro-channel. Since no extra fabrication processes are required for pressure ports, other than traditional ways of making microfluidic devices, the scheme is very scalable.

Finally a"frequency control based pulsing pressure" driving strategy is proposed and implemented for the microfluidic logic devices. The strategy provides a precise control over timing of transport phenomena inside a microfluidic channel. Such a control is only possible via a "digital microfluidic" system which require a very large number of control arrays and a complex fabrication process is involved.

Bibliography

[1] Leonard M. Adleman. Moleculer computation of solutions to combinatorial problems. *Science*, 1994.

[2] Shorya Awtar. *Synthesis and Analysis of Planer Kinematic XY Flexure Mechanisms.* PhD thesis, Massachusetts Institute of Technology, 2004.

[3] Philips Ball. Chemistry meets computing. *Nature*, 2000.

[4] Christopher Earls Brennen. *Cavitation and Bubble Dynamics.* Oxford University Press, 1995.

[5] Nikolas Chronis, Gang L. Liu, Ki-Hun Jeong, and Luke P. Lee. Tunable liquid-filled microlens array integrated with microfluidic network. *Optics Express*, 2003.

[6] D. Cotter, R. J. Manning, K. J. Blow, A. D. Ellis, A. E. Kelly, D. Nesset andI. D. Phillips, and A. J. Poustie andD. C. Rogers. Nonlinear optics for high-speed digital information processing. *Science*, 1999.

[7] Mohamed Gad el Hak. *Flow control : Passive, active, and reactive flow management.* Cambridge Press, 2000.

[8] A. H. Eschenfelder. *Magnetic Bubble Technology.* Springer-Verlag, 1980.

[9] F Z Fang, H Wu, X D Liu, Y C Liu, and S T Ng. Tool geometry study in micromachining. *J. Micromech. Microeng.*, 2003.

[10] Edward Fredkin and Tommaso Toffoli. Conservative logic. *International Journal of Theoretical Physics*, 21:219–253, 1982.

[11] C. R. Friedrich. Micromechanical machining of high aspect ratio prototypes. *Microsystem Technologies*, 2002.

[12] Piotr Garstecki, Howard A. Stone, and George M. Whitesides. Tunable microfluidic bubble generator. 2004.

[13] Peter R. C. Gascoyne, Jody V. Vykoukal, Jon A. Schwartz, Thomas J. Anderson, Daynene M. Vykoukal, K. Wayne Current, Charles McConaghy, Frederick F. Beckera, and Craig Andrews. Dielectrophoresis-based programmable fluidic processors. *Lab on Chip*, (4):299–309, July 2004.

[14] Jose M. Gordilloa, Zhengdong Cheng, Alfonso M. Ganan-Calvo, M. Marquez, and A. Weitz. A new device for the generation of microbubbles. *Physics of Fluids*, 2004.

[15] Saul Griffith. Towards personal fabricators: Tabletop tools for micron and submicron scale functional rapid prototyping. Master's thesis, MIT, 2001.

[16] Carl L. Hansen, Emmanuel Skordalakes, James M. Berger, and Stephen R. Quake. A robust and scalable microfluidic metering method that allows protein crystal growth by free interface diffusion. *Proceedings of National Academy of Sciences*, 99(26):16531–16536, December 24 2002.

[17] H.G.E. Hentschela, C.S. Penceaa, and A. Fineb. Computing with calcium stores and diffusion. *Neurocomputing*, 2004.

[18] N. Michele Holbrook, Maciej A. Zwieniecki, and Peter J. Melcher. The dynamics of "dead wood": Maintenance of water transport through plant stems. *Integrative and Comparitive Biology*, 2002.

[19] Jong Wook Hong and Stephen R Quake. Integrated nanoliter systems. *Nature Biotechnology*, 21(10), 2003.

[20] Jong Wook Hong, Vincent Studer, Giao Hang, W French Anderson, and Stephen R Quake. A nanoliter-scale nucleic acid processor with parallel architecture. *Nature Biotechnology*, 22, 2004.

[21] Susan Z. Hua, Frederick Sachs, David X. Yang, and Harsh Deep Chopra. Microfluidic actuation using electrochemically generated bubbles. *Analytical Chemistry*, 2002.

[22] Klavs Jensen and Abraham Lee. The science & applications of droplets in microfluidic devices. *Lab on Chip*, (4):31–32, 2004.

[23] Mads J. Jensen, Piotr Garstecki, Michael Fuerstman, Henrik Bruus, George M. Whitesides, and Howard A. Stone. Numerical and experimental investigation of bubble pinch-off in flow-focusing device. 2004.

[24] Mads Jakob Jensen, Goran Goranovic, and Henrik Bruus. The clogging pressure of bubbles in hydrophilic microchannel contractions. *J. Micromech. Microeng.*, (14):876–883, May 2004.

[25] Ki-Hun Jeong, Gang L. Liu, Nikolas Chronis, and Luke P. Lee. Tunable microdoublet lens array. *Microstructure devices*, 2004.

[26] Y.S. Leung Ki, M. Kharouf, H.T.G. van Lintel, M. Haller, and Ph. Renaud. Bubble engineering for biomedical valving applications. In *IEEE-BMBS Special Topics conference*, 2000.

[27] Jian Liu, Markus Enzelberger, and Stephen Quake. A nanoliter rotary device for polymerase chain reaction. *Electrophoresis*, (23):1531–1536, 2002.

[28] Seth Lloyd. Any nonlinear gate with linear gates suffices for computation. *Physics Letters A*, (167):225–260, 1992.

[29] Goodwin M. Micro fluidic control systems in deep etch optical lithography. *Microsystems Technologies*, pages 197–200, 1998.

[30] Bakhtiar Mikhak, Christopher Lyon, Tim Gorton, Neil Gershenfeld, Caroline McEnnis, and Jason Taylor. Fablab : An alternate model of ict for development. In *Internation Conference on Development by Design*, 2002.

[31] A. Ney, C. Pampuch, R. Koch, and K. H. Ploog. Programmable computing with a single magnetoresistive element. *Nature*, 2003.

[32] Y.N. Picard, D.P. Adams, M. Vasile, and M. Ritchey. Focused ion beam-shaped microtools for ultra-precision machining of cylindrical components. *Precision Engineering*, 2003.

[33] Alberto Pique and Douglas B. Chrisey. *Direct-Write Technologies for rapid prototyping applications : Sensors, Electornics and Integrated Power sources.* Academic Press, 2002.

[34] Ronald F. Probstein. *Physochemical Hydrodynamics : An introduction.* Butterworths, 1989.

[35] Vijay Srinivasan, Vamsee K. Pamula, and Richard B. Fair. An integrated digital microfluidic lab-on-a-chip for clinical diagnostics on human physiological fluids. *Lab on Chip*, (4), May 2004 2004.

[36] Andrew Steane. Quantum computing. 1997.

[37] Todd Thorsen, Sebastian J. Maerkl, and Stephen R. Quake. Microfluidic large-scale integration. *Science*, 2002.

[38] Todd Thorsen, Richard W. Roberts, Frances H. Arnold, and Stephen R. Quake. Dynamic pattern formation in a vesicle-generating microfluidic device. *Physics Review Letters*, 86(18):4163–4166, April 2001.

[39] Agota Toth and Kenneth Showalter. Logic gates in excitable media. *J. Chem. Phys.*, 1995.

[40] Igor Turovets, Daniel Palanker, Itzhak Hemo, and Aaron Lewis and. Dynamics of cavitation bubble induced by 193 nm arf excimer laser in concentrated sodium chloride solutions. *Journal of Applied Physics*, 1996.

[41] Marc A. Unger, Hou-Pu Chou, Todd Thorsen, Axel Scherer, and Stephen R. Quake. Monolithic microfabricated valves and pumps by multilayer soft lithography. *Science*, 288, april 2000.

[42] K. Vanheusden, W.L. Warren, R.A.B Devine, D.M. Fleetwood, J.R.Schwank, M.R.Shaneyfelt, P.S. Winokur, and Z.L. Lemnios. Non-volatile memory device based on mobile protons in sio2 thin films. *Nature*, 386, 10 April 1997.

[43] T Vestad, D W M Marr, and J Oakey. Flow control for capillary-pumped microfluidic systems. *Journal of Micromechanics and Microengineering*, 2004.

[44] Ying-Chih Wang, Man Ho Choi, and Jongyoon Han. Two-dimensional protein separation with advanced sample and buffer isolation using microfluidic valves. *Anal. Chem.*, 76(15):4426–4431, August 2004.

[45] George Whitesides and Abraham D. Stroock. Flexible methods for microfluidics. *Physics Today*, 2001.

[46] Eric J. Wilhelm. *Printed Electronics and Micro-electromechanical Systems.* PhD thesis, MIT, 2004.

[47] Bo Zheng, L. Spencer Roach, and Rustem F. Ismagilov. Screening of protein crystallization conditions on a microfluidic chip using nanoliter-size droplets. *Journal of American Chemical Society*, (125):11170– 11171, August 2003.

[48] Maciej A. Zwieniecki, Peter J. Melcher, and N. Michele Holbrook. Hydrogel control of xylem hydraulic resistance in plants. *Science*, 2001.